Delft University of Technology

TNO
Quantum Technology Department

Master Thesis

Development of Josephson Parametric Amplifiers for quantum applications

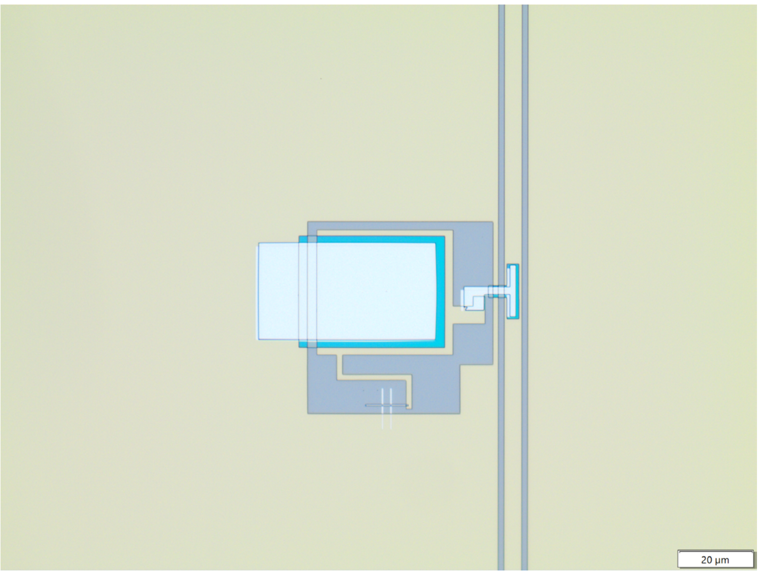

Author :
Ing. Stefanos Basili

To be defended publicly on Wednesday October 26th, 2020 at 09:30 AM.

Student number:	4541057	
Project duration:	February 10, 2020 – October 10, 2020	
Thesis committee:	Prof. dr. ir. G. Steele,	TU Delft, supervisor
	Prof. dr. ir. S. Otte,	TU Delft
	Dr. ir. S. Goswami,	TU Delft
Daily Supervisors:	Ir. R. Vollmer,	TNO
	Dr. ir. T. Last,	TNO
	Dr. ir. A. Bruno,	TU Delft

Preface

These then are some illustrations of things that are happening in modern times – the transistor, the laser, and now these junctions, whose ultimate practical applications are still not known.
The quantum mechanics which was discovered in 1926 has had nearly 40 years of development, and rather suddenly it has begun to be exploited in many practical and real ways.
We are really getting control of nature on a very delicate and beautiful level.
— Richard P. Feynman —

Acknowledgements

This year has been a rollercoaster in which I had the opportunity of meeting and working with great people.

First, I want to thank **Thorsten Last** for allowing me to work at TNO on this ambitious project. I also want to thank **René Vollmer**, who acted as daily supervisor. I am very grateful for your guidance throughout the project. Whenever I had a question about the theory (whether it is about electrical engineering, quantum mechanics, programming and many more), you always made time to give me a crystal clear explanation. I also want to thank you for making the scattering matrix simulation used to understand the JTWPA transmission measurements. I want to thank **James Kroll** for the cryogenic measurements he did on my devices. Even though we worked together briefly, I was able to learn a lot about low-temperature and microwave measurements. I want to thank **Larysa Tryputen** for the helpful discussions about fabrication. I want to thank all the people in the QT department of TNO for making the work environment a pleasurable experience.

Furthermore, I want to thank **Prof. Gary Steele** for steering the project to the right direction and for all the helpful discussions and explanations. I would also like to thank **Sarwan**, **Adrián** , **Jasper**, **Yildiz** and **Fatemeh** from the Steele lab, for their help and advice when I needed to do the cryogenic measurements together with James.

Lastly, I want to acknowledge **Alessandro Bruno** for supervising me in the cleanroom and for making the designs for the devices. You, together with **Nandini** and **Christos**, were always around to help me with the fabrication. Without your input and supervision, this project would not have been what it is. I'm excited to continue to work with you as intern at your new start-up company QuantWare.

Of course, I also want to thank my family and friends, for helping me through some lonely hours in the cleanroom by face timing me every now and then.

-Stefanos Basili, Delft, September 2020

Abstract

Quantum-limited parametric amplifiers have become increasingly interesting and relevant with the progressing field of quantum computing. However, currently it is still challenging to fabricate these complex devices. In this thesis, we developed cross type Josephson junctions (JJs), lumped element LC resonators, lumped element Josephson parametric amplifiers (JPAs) and Josephson traveling wave parametric amplifiers (JTWPAs). We found and resolved several fabrication issues however we suspect that both the JPA and JTWPA suffered from microshorts in the circuits during the cryogenic measurements. Nevertheless, we managed to measure the resonance frequency of the JPA and have noticed the flux focusing effect when we flux tune it. We preformed room temperature measurements on over 300 JJs and calculated the relative standard deviation (RSD) for various JJ sizes. We found the spread of 30 fabricated resonators and a rough estimate of their Q factors. The JTWPAs developed are non-degenerate four wave mixing amplifiers that use the resonant phase matching (RPM) technique to reduce the phase mismatch problem. The transmission through the measured JTWPA showed 50 dB loss probably caused by presumably a short from the transmission line to ground. However, when the JTWPA was driven with a pump we observed 20 dB increase in transmission in some frequency bands.

Contents

List of Symbols

Table 1: List of symbols used in this thesis, their meaning and (if applicable) the units in which they are commonly expressed.

Meaning	**Symbol**	**Unit**
Inductance	L	H
Capacitance	C	F
Resistance	R	Ω
Impedance	Z	Ω
Voltage	V	V
Guidance	G	S
Scattering parameter	S	dB
Inductance per unit length	L_l	H/m
Capacity per unit length	C_l	F/m
Resistance (conductor) per unit length	R_l	Ω/m
Guidance (dielectric) per unit length	G_l	S/m
Current	I	A
Critical temperature	T_c	K
Angular frequency	ω	rad/s
Frequency	f	Hz
Time	t	s
Phase	ϕ	rad
Quality factor (Q-factor)	Q	-
(Energy)loss rate	κ	s^{-1}
Bandwidth	BW	Hz
Magnetic flux	Φ	Wb
Phase difference	$\Delta\phi$	rad

1

Introduction

This is an external master thesis on the subject of parametric amplifiers performed at TNO in the Quantum Technology department. This thesis is part of existing research within the group of Prof. Dr. Ir. Gary Steele, which is part of the Quantum Nanoscience department of the Applied Sciences faculty of the Technical University of Delft. This chapter aims to introduce the reader to the field interest and explain the goal of the thesis.

1.1. Quantum-limited amplification

Richard Feynman is probably the first scientist who theorized the quantum computer [13]. Quantum computing remains currently the most popular and promising application of quantum technology. It has emerged from a long search for more efficient ways to process information when quantum mechanics made it to the scope of the research [29]. Quantum computers use two-level systems referred to as quantum bits or qubits. Qubits have quantum mechanical abilities like being in a superposition or entangled state. To have qubits operating in those states the quantum computer is required to be at a low energy scale. Therefore we need the system to be in low temperatures, which hinders the control and readout of the qubits which is usually performed via an microwave signal. The power of such a signal consists typically of a few photons and hence has an energy of a few femtowatts. However, the electronics used to control the signals sent to the quantum chip as well as the readout of the signals coming out are placed at room temperature. The signal powers room temperature machines operate with is of the order of milliwatt. This shows the need for an amplification chain between the quantum chip and the room-temperature electronics which is an issue for almost all quantum technologies operated at low temperatures. Naturally we live in a non-ideal world where there is always some noise added to the signal when it propagates through a component. The added noise can not be completely removed, a limitation imposed by quantum mechanics itself [11] prevents this. This has then led to the pursuit of parametric amplifiers who can reach this quantum-limit.

1.2. Goal

Quantum-limited amplifiers have become increasingly interesting and relevant to the progressing fields of quantum computing. However, it is still challenging to fabricate such complex devices, as these devices rely on a large number of well-targeted and functional nano-scale objects called Josephson junction. These parametric amplifiers are fabricated on planar chips inside of the cleanroom. In addition to the Josephson junction, such amplifiers also require more fundamental components such as transmission lines and LC-resonators. The challenge is to find a valid way to fabricate, measure and characterize each component both individually as well as connected together, as one device. This research included a couple of feedback loop cycles in the design, fabrication, and characterization of Josephson parametric amplifiers, Fig. 1.1. The outcome of this thesis can be used as initial fabrication procedures for making quantum-limited Josephson parametric amplifiers.

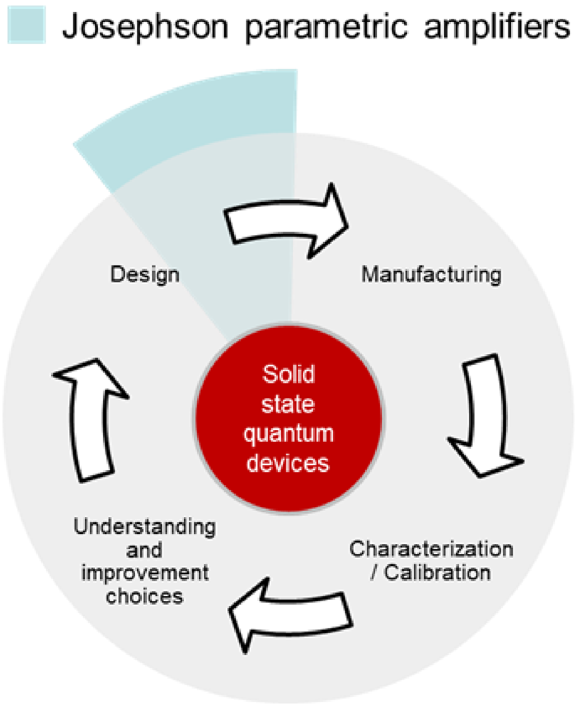

Figure 1.1: Feedback loop for this project

2

Theory

This chapter aims to give the reader some understanding of the relevant theories and concepts. First, there is a short section about amplifiers and parametric amplifiers. After this, another section will discuss microwave engineering and relevant theories, since signals that are being amplified and measured are in the microwave domain. Then there is a section about superconductivity in particularly the Josephson effect and junction are described because the amplifiers built in the project consist typically out of those junctions. Finally, there is a part about Josephson parametric amplifiers and Josephson traveling-wave parametric amplifiers. The theory would be kept brief and general just to understand the results of this thesis, as this thesis is experimental rather than theoretical.

2.1. Amplifiers

A quantum processor is an extremely fragile system. States of the qubits inside a quantum processor can collapse by a tiny disruption. Therefore the signal used in quantum computing is usually in the order of a few photon energy in a very cold environment ($k_b T$). Sending a very weak signal through a quantum processor one might understand that the readout signal needs not only to be amplified with a high enough gain but also with the lowest noise as possible. This is where amplifiers come into the picture.

2.1.1. Transistor-based amplifiers

The most basic amplifier is a transistor amplifier. The DC bias voltage applied to the emitter base junction V_{EB}, makes it remain in forward biased condition. This forward bias is maintained regardless of the polarity of the signal coming from V_I. Fig. 2.1 shows how a transistor looks like when connected as an amplifier.

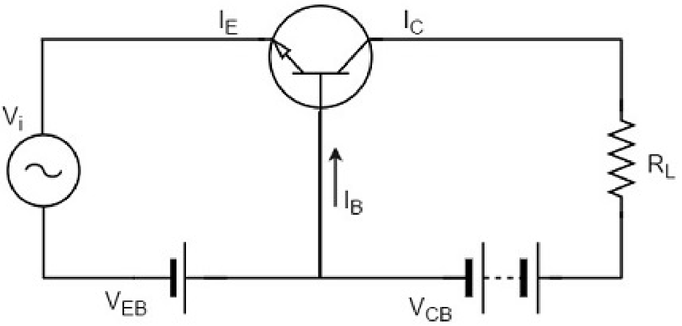

Figure 2.1: Circuit of a typical transistor amplifier.

The low resistance in input circuit, lets any small change in input signal to result in an appreciable change in the output. The emitter current I_E caused by the input signal contributes the collector current I_C, which when flows through the load resistor R_L, results in a large voltage drop across it. Thus a small input voltage results in a large output voltage, which shows that the transistor works as an amplifier. The figures of merit of an amplifier are numerical measures that characterize its properties and performance. Figures of merit can be given as a list of specifications that include properties such as:

- Gain. The gain of an amplifier is the ratio of output to input power or amplitude, and is usually measured in decibels. When measured in decibels it is logarithmic scaled related to the power ratio: $G(\mathrm{dB}) = 10\log(P_{out}/P_{in})$.
- Bandwidth. The bandwidth of an amplifier is the range of frequencies for which the amplifier gives "satisfactory performance". The definition of "satisfactory performance" may be different for different applications. However, a common and well-accepted metric is the half-power points (i.e. frequency where the power goes down by half its peak value) on the output vs. frequency curve. Therefore, bandwidth can be defined as the difference between the lower and upper half power points. This is therefore also known as the 3 dB bandwidth.
- Noise. Noise is an unwanted signal that creates disturbance to the desired signal content in the system. This can be an additional signal that is produced within the system or can be some disturbance accompanied with the desired information of the input signal. However, it is unwanted and has to be removed. A good system is one in which the noise generated by the amplifier itself is small compared to noise from the incoming source.

Figures of merit are important for determining the suitability of a particular amplifier for an intended use. For quantum computing, the traditional method has become amplifying with amplifiers based on high-electron-mobility transistors (HEMT's) [42]. These amplifiers have high mobility which stems from the fact that the transistor uses a hetero-junction. Unlike the p-n junction, it uses different materials on both sides of the junction. The different bandgap energies of the materials create a quantum well where the electrons are confined, where scattering from impurities can be avoided. HEMT amplifiers have been used with cryogenic cooling in quantum computing and radio astronomy to reduce the noise, up to 4-5 times the quantum limit at around 50 GHz [7].

2.1.2. Parametric amplifiers

However having just a HEMT in the amplification chain still results in a low signal to noise ratio (SNR) in quantum computing. To overcome the limitations of the HEMT a different type of amplifier is used, known as a parametric amplifier, or paramp. Paramps use some kind of energy source to modulate a parameter of a dynamical system to add energy to the signal desired to be amplified. Parametric amplification does not require any energy dissipation, making it possible for them to reach quantum-limited noise performance [8]. A reduction of the noise by a factor of 4-5 is very preferable. In general, to get parametric amplification of a signal, it has to be amplified in the presence of a pump signal in a medium with nonlinear components, see Fig. 2.2.

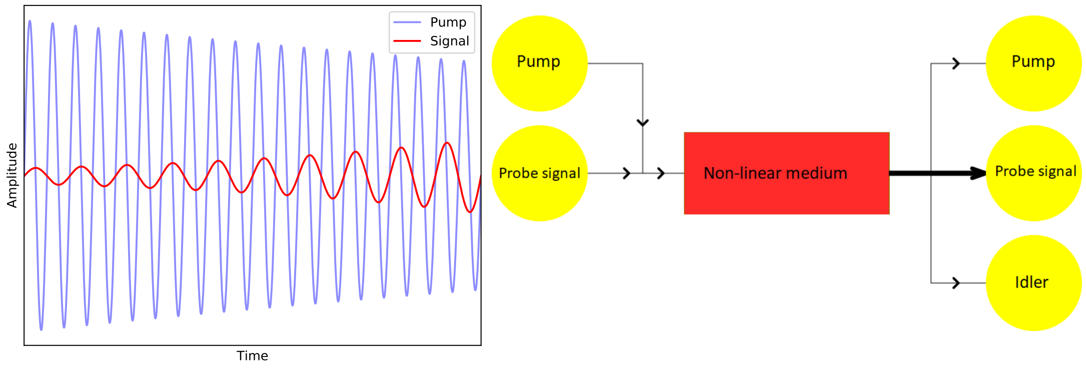

Figure 2.2: The amplitude of the signal oscillation is increased (driven) by a periodically varying system parameter ($\omega_p = 2\omega_s$) demonstrating parametric amplification (left).A schematic of parametric amplification (right).

The paramp has two inputs, the signal that has to be amplified with frequency ω_s and the pump signal that supplies energy to the probe signal with frequency ω_p. Those two signals propagate through a nonlinear medium where the pump and the signal can interact. The nonlinearity in this medium is introduced by the Josephson junctions, discussed in section 2.3.1. The system will give rise to a third signal called the idler with frequency ω_i due to energy and phase conservation. Two different amplification processes can take place, either three- or four-wave mixing. In the three-wave mixing process, one pump photon is converted in one signal and one idler photon. In the four-wave mixing process, two pump photons are converted to one signal and one idler photon. Suppose the amplified signal and idler signal are equal ($\omega_s = \omega_i$) then the process is called a degenerate process which is phase-sensitive. With this mode, it is possible to achieve noiseless amplification of the amplitude of the signal, but the phase-information will be lost [38]. If this is not the case ($\omega_s \neq \omega_i$) the process is phase-insensitive also known as non-degenerate. In this mode half a noise photon is added (i.e. quantum limit) [38]. See table 2.1 for a overview of different parametric amplification.

Table 2.1: Summary of the different ways of parametric amplification.

	Three-wave mixing	**Four-wave mixing**
Degenerate amplification	$\omega_p = \omega_s + \omega_i$, $\omega_s = \omega_i$, $2\omega_s = \omega_p$	$2\omega_p = \omega_s + \omega_i$,$\omega_s = \omega_i = \omega_p$
Non-degenerate amplification	$\omega_p = \omega_s + \omega_i$,$\omega_s \neq \omega_i$	$2\omega_p = \omega_s + \omega_i$, $\omega_s \neq \omega_i$

The devices fabricated in this thesis operate with a non-degenerate four-wave mixing process. Three-wave mixing can also be used for parametric amplification [37] however it has not been studied in this thesis. In three-wave mixing, the signal and idler frequency add up to the pump frequency. When the signal is at exactly half the pump frequency (degenerate amplification), signal and idler will have the same frequency allowing them to interfere. This gives phase-sensitive amplification. When the signal is not at half the pump frequency, the idler ends up at a different frequency (non-degenerate amplification). In the four-wave mixing case, the pump frequency is at half the sum of the signal and idler frequencies. Degenerate amplification will in this case be problematic as signal, idler and pump would all have the same frequency [38].

2.2. Microwave engineering

This section will give a brief overview of some microwave theory relevant to this thesis. Background and more detailed information can be found in textbooks such as [10] and [34].

2.2.1. LC circuits

An LC circuit is an electrical circuit, which consists of an inductor (L) and a capacitor (C).

Figure 2.3: Circuit diagrams of a serie (left) LC oscillator and (right) LCR oscillator.

This type of circuits is present in nearly all electronic equipment in many forms. Big equipment, like classical radios, have electronic components that are discrete devices connected. In this thesis, the electronic components are fabricated on the planar surface of a silicon chip. Despite many forms of electronic components, the basic properties of an LC circuit remain the same and are generally depicted schematically by the lumped circuit diagram of Fig. 2.3.

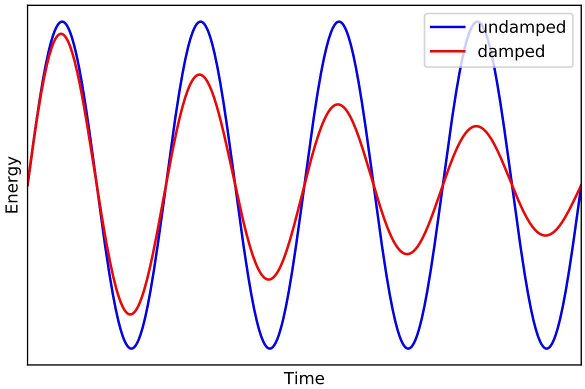

Figure 2.4: Damped (RLC) and undamped (LC) oscillations graph plotting energy as an function of time.

The LC circuit can be excited at a specific frequency (ω_0). The current through the circuit is sinusoidal in time which can be expressed as:

$$I = I_0 \cos(\omega_0 t + \phi) \tag{2.1}$$

with an amplitude I_0 and phase offset ϕ. By neglecting the electrical resistance (R), it is assumed that there is no energy loss in the circuit. The LC circuit is therefore the idealized form of the RLC circuit, in which resistance does play a role. Once the LC circuit is energized it will oscillate forever at its resonance frequency ω_0 which is given by

$$\omega_0 = 1/\sqrt{LC} \tag{2.2}$$

where L is the inductance and C the capacitance. When this circuit is energized, for example by charging the capacitor, the energy periodically flows from the capacitor to the coil and vice versa. In the more realistic case, there will be some resistance that damps the oscillation. The dissipative electric components are often grouped in a single resistor, as shown in Fig. 2.3. An RLC circuit will have the same resonance frequency as the LC circuit but without a force driving it, the oscillation amplitude will decay over time due to losses, see Fig. 2.4. A common measure of these losses is the quality factor (Q-factor) [34]. The Q-factor is a dimensionless parameter that describes how damped an resonator is. Higher Q indicates a lower rate of energy loss (κ) and so the resonators have low damping which makes them vibrate longer.

$$Q = \frac{\omega_0}{\kappa} = \frac{\omega_0}{BW} = \frac{\omega_0}{\omega_2 - \omega_1} \tag{2.3}$$

It can also be defined as the ratio of the resonate frequency to its bandwidth (BW). The common cut-off for the oscillation amplitude is the half-power point. The two points (ω_1, ω_2) in Fig. 2.5 are where the oscillation frequencies contain half the power of the oscillations at the resonant frequency ω_0. The frequency interval between those two points is the bandwidth.

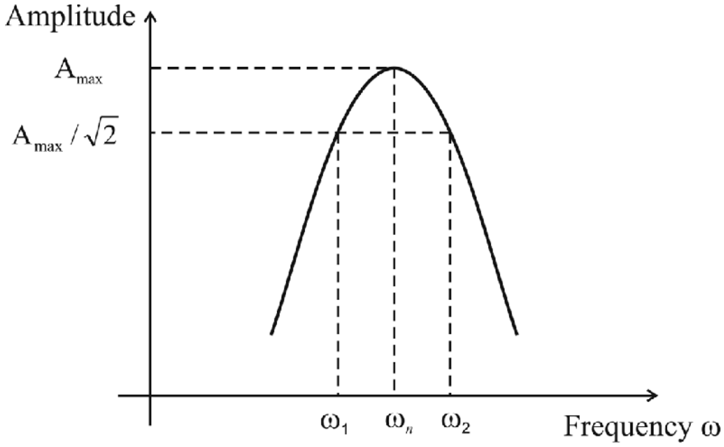

Figure 2.5: Oscillation amplitude in frequency domain for an RLC circuit.

Basic circuit analysis deals with lumped elements where physical quantities like R, C and L do not vary over the physical dimension of the elements. It assumes the wavelengths to be much longer than the elements they propagate through. In this thesis distributed elements like transmission lines are used, for which basis circuit analysis is an invalid assumption as the wavelengths are comparable with the dimensions of the electrical elements developed. The microwave transmission line theory is a better analysis theory for these electrical structures.

2.2.2. Microwave transmission line

Transmission line theory bridges the gap between field analysis and basic circuit theory and therefore is of significant importance in the analysis of microwave circuits and devices [10]. The main difference between circuit theory and transmission theory is system size. Microwaves are typically in the range of 3-300 GHz, corresponding to wavelengths of 100 mm to 1 mm. Thus making the transmission line vary in voltage and current over its length. This wavelike behavior of a transmission line is described by the telegraph equations, which can be derived from Maxwell's equations and Kirchhoff's laws. An approximation per unit length of the transmission line (L_l, C_l, R_l and G_l, table 1) needs to be used, see Fig. 2.6.

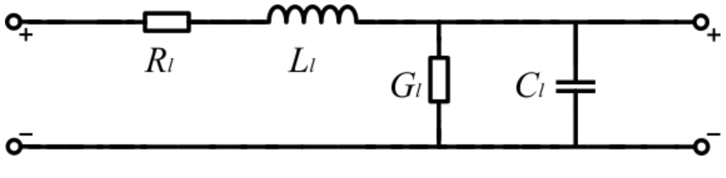

Figure 2.6: Lumped element model of a transmission line consisting of two conductors (wires) of opposite polarity with a homogeneous cross section relative to the conductors.

A transmission line can, instead of the fundamental parameters, also be characterized by more intuitive parameters like the characteristic impedance:

$$Z_0 = \sqrt{\frac{R_l + i\omega L_l}{G_l + i\omega C_l}} = V/I \tag{2.4}$$

The characteristic impedance reduces to,

$$Z_0 = \sqrt{\frac{L_l}{C_l}} \tag{2.5}$$

if the transmission line is assumed to be lossless (so $R = G = 0$).
Instead of directly driving the oscillators with a voltage or current source, like Fig. 2.3 it is common to couple the oscillators to a transmission line. In the next section is explained how a coupled parallel LC resonator to a transmission line behaves.

2.2.3. Microwave LC resonator capacitively coupled to a transmission line

At frequencies near resonance, a microwave resonator can be modeled as a parallel LC lumped-element resonant circuit. There are multiple ways to couple an LC resonator to a transmission line but the most relevant for this research is the capacitively coupled method. In the capacitively coupled case, the transmission line is coupled to the circuit through a capacitor, see figure below.

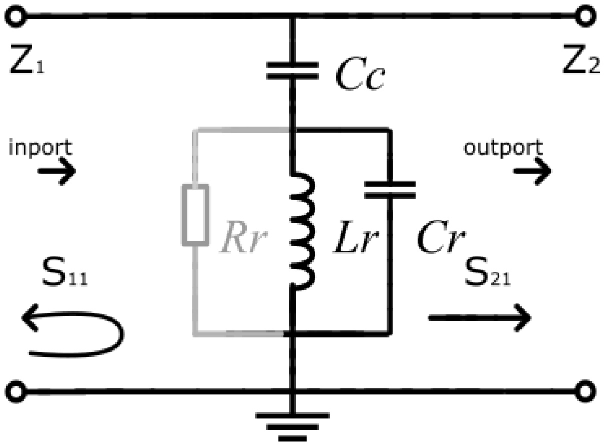

Figure 2.7: Parallel (R)LC lumped-element circuit coupled capacitively to the transmission line. The resistive part is blurred out.

If a signal is sent from the left side through the transmission line to the LC resonator, it can either be reflected back or transmitted through. These two fractions of power, usually denoted as S_{11} for reflection and S_{21} for transmission, are called the scattering parameters. Scattering refers to the way in which the traveling signal in the transmission line is affected when it meets a discontinuity caused by an impedance differing from the line's characteristic impedance. S-parameters are represented in matrix form also known as the scattering matrix. The scattering matrix relates the signals incident on the ports to those reflected from the ports. It provides a complete description of the network as seen at its N ports (N=2 in Fig. 2.7). For a capacitively coupled LC circuit, the scattering parameters can be calculated using network analysis techniques. The network can be modulated as two oscillators, the LC resonator (internal) and the "leaking out" of the signal to the transmission line (external). The total quality factor is composed out of the internal and external quality factors

$$\frac{1}{Q_{tot}} = \frac{1}{Q_{int}} + \frac{1}{Q_{ext}} \tag{2.6}$$

Q_{ext} depends on the coupling capacitance (C_c) and the characteristic impedance of the circuit, while the Q_{int} depends only on the resistance which is usually fixed in nano-structures by the choice of material. Calculating the scattering parameters gives insight on how the system should respond to a certain signal. The response can be characterized in three cases:

- Under coupled: Most of the loss happens inside the LC resonator, $Q_{ext} > Q_{int}$ (usually the case for RLC resonators).
- Critically coupled: The loss inside the LC resonator is equal the losses to the transmission line, $Q_{int} = Q_{ext}$. However this type is not usual.
- Over coupled: Most of the loss happens inside the transmission line, $Q_{ext} < Q_{int}$.

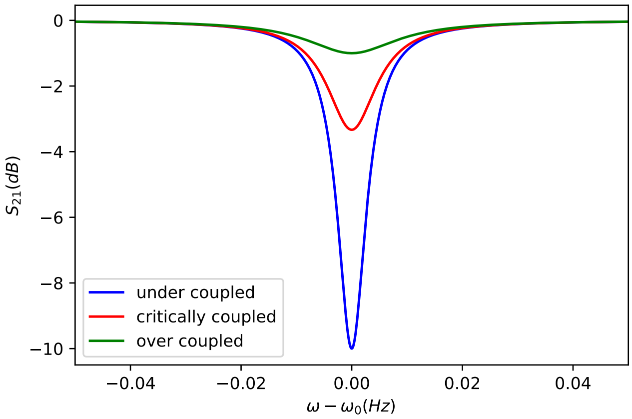

Figure 2.8: The transmission scattering parameters of the LC resonant circuit (Fig. 2.7) is shown. For the three lines, three different values of Q_{int} are shown, while ω_0 and the bandwidth are held constant.

Fig. 2.8 below shows what could be expected if the coupled resonator is measured with a VNA (vector network analyzer) for transmission S_{21}.

The transmission coefficient shows a dip at the resonance frequency labeled as $S_{21,min}$. The Q-factor and the minimum transmission at resonance are given with

$$| S_{21,min} |= \frac{Q_{tot}}{Q_{int}} \tag{2.7}$$

where Q_{int} is the internal Q-factor [26]. This expression together with Eq. 2.6 can be used to extract the external Q-factor. This formula can be used for a rough estimate. However for the data fitting of the measurements calculations involving a complex valued Q-factor were used [21].

2.2.4. Coplanar waveguide

The purpose of a transmission line is to transmit signals from point A to point B with as little loss as possible. A well-known example of a conventional transmission line is a coax cable. However in electronics, the coplanar waveguide (CPW) is used as on-chip microwave transmission line. This is an on-chip planar transmission line and like the coax cable, it is used to convey microwave-frequency signals. The CPW consist of a single conducting track on silicon (Si). The track is separated from the rest of the conducting film with a small gap. The film on the 525μm Si wafer is in our case 100nm niobium titanium nitride (NbTiN). This (super)conducting film is chosen because of its low oxidation rate and high critical temperature (superconductivity will be explained in the next section section 2.3).

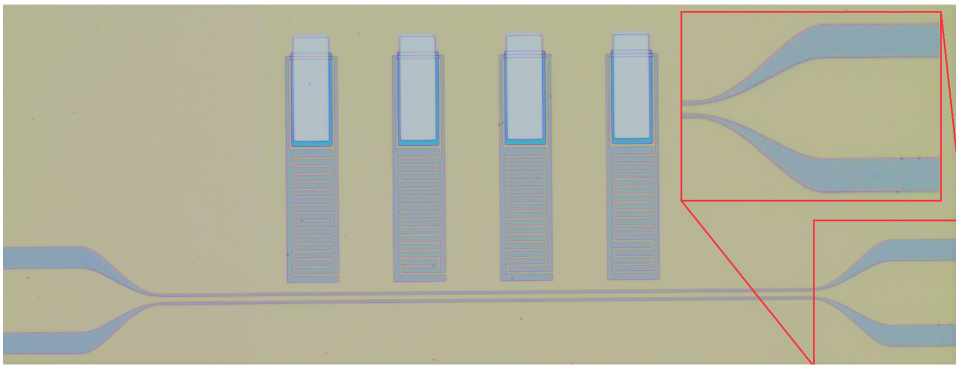

Figure 2.9: CPW with four LC resonators coupled to it and a zoom in of the smooth taper.

The microwave resonators and other devices fabricated in this thesis are coupled to a CPW. The CPW is employed as input and output lead. The characteristic impedance should be constant throughout the whole CPW and the rest of the readout system, to prevent reflections. To do so a smooth CPW taper (or launcher) is used at both ends of the transmission line of the devices [22], see Fig. 2.9. The CPW should also be designed and fabricated in a way that it has the right capacitance per unit length and inductance per unit length. The capacitance per unit length of a coplanar waveguide can be calculated using conformal mapping and involves elliptical integrals [34]. There are finite element simulation tools available to calculate this for certain geometries. The coplanar waveguide used in this thesis has been simulated with SONNET to obtain the desired characteristic impedance of 50 Ω. Three properties need to be understood to be able to find realistic parameters needed for the SONNET simulation, the kinetic inductance of the thin film and the inductance and capacitance per unit length. The CPW is important for us as it is the feedline of some devices fabricated in this thesis.

Kinetic inductance

The first important property is the kinetic inductance. Kinetic inductance is the manifestation of the inertial mass of mobile charge carriers like Cooper pairs in alternating electric fields as an equivalent series inductance [3]. Kinetic inductance is observed in high carrier mobility conductors like superconductors (superconductors are explained in section 2.3). The sheet kinetic inductance is given with the following expression

$$L_{k,s} \simeq \frac{\hbar R_s}{\pi \Delta} \tag{2.8}$$

where R_s is the sheet resistance in the non-superconducting state, Planck constant is $\hbar = \frac{h}{2\pi} = 1.054571817 \cdot 10^{-34} Js$ and Δ is the superconducting energy gap ($\Delta = 1.76 k_B T_c$) [3]. This equation is valid at $T \ll T_c$ and $f \ll \Delta/h$.

The resistance is a important property of the NbTiN film. For a rectangular piece the resistance is given by

$$R = \frac{\rho \cdot l}{w \cdot t} \tag{2.9}$$

where ρ is the resistivity at room temperature, l the length, w the width and t the thickness of the film [14]. If a square piece is considered ($l = w$) the sheet resistance is found to be

$$R_s = \rho / t \tag{2.10}$$

in units of ohms per square [14]. After fabricating the any thin conducting film (NbTiN in this thesis) on a substrate (Si wafer) a 4 point probe measurement (for sheet resistance R_s) and profilometer measurement (for thickness film t) are done to determine the resistivity of the film. Notice that R_s and $L_{k,s}$ are both sheet values for one square of a thin conducting film and both are independent of the square size.

Inductance and capacitance per unit length

As explained in section 2.2.2 the CPW has an inductance and capacitance per unit length. In the CPW model, the total series inductance per unit length consists of two parts namely the kinetic inductance (also referred to as internal inductance per unit length $L_{k,l}$), which accounts for magnetic energy storage within the conductor, and the external inductance per unit length $L_{g,l}$, which account for magnetic energy storage external to the conductor [34]. So Eq. 2.5 can be expressed as

$$Z_0 = \sqrt{\frac{L_{k,l} + L_{g,l}}{C_l}}. \tag{2.11}$$

The (internal and external) inductance and capacitance per unit length are given by

$$L_{g,l} = \frac{\mu_0 K(\sqrt{1-k^2})}{4K(k)} \tag{2.12}$$

$$L_{k,l} = L_{k,s}(g_g + g_c) \tag{2.13}$$

$$C_l = 4\epsilon_0 \epsilon_{eff} \frac{K(k)}{K(\sqrt{1-k^2})} \tag{2.14}$$

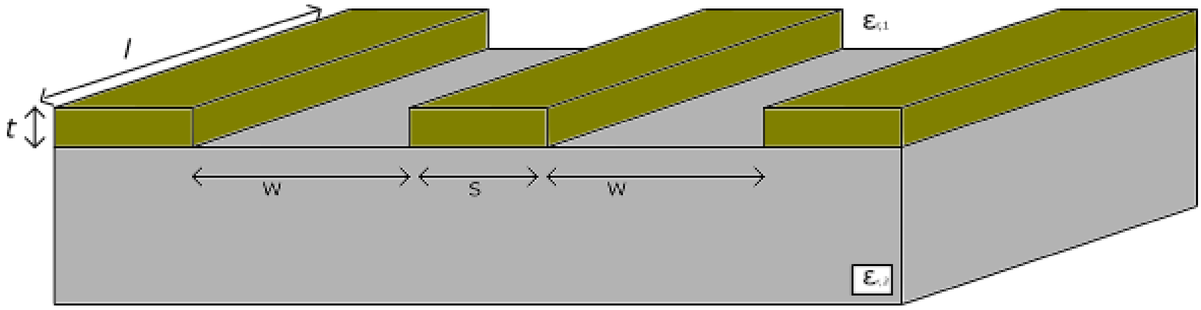

Figure 2.10: Schematic representation of the cross-section of a CPW.

with

$$k = \frac{S}{S+2W} \tag{2.15}$$

(see Fig. 2.10 for dimension parameters S and W), the vacuum permittivity constant ϵ_0 and the vacuum permeability constant μ_0. A CPW line is deposited on a dielectric substrate. The electric field of the CPW will be partly in vacuum, and partly on the dielectric substrate. To model this effect the system can be seen as CPW in a homogeneous effective dielectric which has a relative permittivity or dielectric constant given by

$$\epsilon_{eff} = \frac{\epsilon_{r,1} + \epsilon_{r,2}}{2} \tag{2.16}$$

where $\epsilon_{r,1}$ and $\epsilon_{r,2}$ are the dielectric constants of the media above and below the CPW, respectively. In the case of the CPW fabricated in this thesis the medium above the CPW is vacuum ($\epsilon_{r,1} = 1$) and the dielectric constant of the silicon substrate $\epsilon_{r,2}$ is 11.44, so $\epsilon_{eff} = 6.22$. To convert $L_{k,s}$ into the kinetic inductance per unit length $L_{k,l}$, the geometric contributions of the central line and ground plane (g_g and g_c) [16] are calculated. K is the complete elliptical integral of the first kind which is typically evaluated in a numerical solver. In this thesis, Matlab is used as solver for this integral which occurs in the geometric contributions, the external inductance per unit length and the capacitance per unit length.

2.2.5. Impedance matching

So the transmission line has certain high-frequency properties such as characteristic impedance and resonance frequencies. Due to these properties, engineers strive to place appropriate impedance matched elements on the line. If this is done incorrectly, signal loss or distortion may occur due to reflections between the line. The reflected power is given by the reflection coefficient R_P which is given by

$$R_P = \mid S_{11} \mid^2 = \left| \frac{Z_2 - Z_1}{Z_2 + Z_1} \right|^2 \tag{2.17}$$

If the two elements have the same characteristic impedance, the impedance is matched and there is no reflection ($Z_1 = Z_2$), while if there is a difference, the impedance is mismatched and non-zero reflection is obtained, see Fig. 2.7 as example. The S_{21} scattering parameter directly relates to the impedance matching as well as the transmission from the IN-port to the OUT-port.

At low temperatures the conductance of a semiconductor is espected to be zero. When no resistive elements are included in the lumped-element representation of the circuit the total quality factor is equivalent to the external quality factor ($Q_{ext} = Q_{tot}$), according to Eq. 2.6. The quality factor is then determined by the internal reflections caused by off-target electrical components. The system has to be cooled down to a few Kelvin above absolute zero to reach this state. This is done with large and expensive installations which usually use liquid helium to cool the system down. The next section will cover superconductivity and some concepts involving this phenomenon.

2.3. Superconductivity

Superconductivity is the quantum phenomenon at which the electrical resistance of some materials below a certain critical temperature T_c suddenly disappears completely. The phenomenon was discovered on April 8, 1911, in Leiden by Heike Kamerlingh Onnes [31]. When the material goes into its superconducting state, electrons pair up in so-called Cooper-pairs. Then they form a superconducting condensate, which can be described by a single wave function with an amplitude and a phase describing all the electrons in the condensate. Interesting and useful concepts and applications arising from superconductivity are explained in this section.

2.3.1. Josephson junction

A Josephson junction (JJ) consists of two superconductors with between them a weak link where tunneling of electrons and cooper pairs occur. This is called the Josephson effect. It was discovered by Brian Josephson for which he received the Nobel Prize in Physics in 1973 [19]. There are lots of variations of the weak link but the junctions used in this thesis use an oxide thin layer as an insulator. For a broader explanation, the reader is referred to [5]. In this book, the following two relations for an ideal JJs are derived

$$I_J = I_c \sin(\Delta\phi) \tag{2.18}$$

$$V_J = \frac{\Phi_0}{2\pi}\frac{\partial\Delta\phi}{\partial t} \tag{2.19}$$

where I_J is the current through the JJ, V_J is the voltage over it, $\Phi_0 = h/(2e)$ is the reduced superconducting magnetic flux quantum, $\Delta\phi$ is the phase difference of the wave functions of the two superconductors and I_c is the critical current. For a constant phase difference ($V_J = 0$), there may still be a current through the JJ ($I < I_c$), consisting of tunneling Cooper pairs referred to as supercurrent. This is called the DC (Direct Current) Josephson effect. As soon as the current exceeds the critical current of the JJ $I > I_c$, superconductivity breaks, a voltage appears and the junction changes into a resistive state. The critical current, for each individual JJ, can be inferred using the Ambegaokar-Baratoff relation [2] by measuring the room temperature resistance also known as the normal state resistance R_n. The relation is given by the following equation

$$I_c = \frac{\Delta_1(T)}{R_n} K\left(\sqrt{1-\frac{\Delta_1^2(T)}{\Delta_2^2(T)}}\right) \tag{2.20}$$

where $\Delta_1(T)$ is the lower, and $\Delta_2(T)$ the higher superconducting energy band gaps of the involved electrodes (in eV) and K the complete elliptical integral of the first kind. In case of $\Delta_1(T) = \Delta_2(T)$, $K(0) = \frac{\pi}{2}$ which reduces the equation to

$$I_c = \frac{\Delta_1(T)}{R_n}\frac{\pi}{2}. \tag{2.21}$$

where the superconducting bandgap energy is given with $\Delta = 1.76 k_B T_c$ in which T_c of aluminum is 1.25 K. With this relation, fast room temperature measurements of the resistance can give estimations of the critical current of a single junction.

2.3.2. Josephson inductance

The Josephson relations (2.18 and 2.19) give rise to a nonlinear inductance L_J called the Josephson inductance. In general, inductance describes how much an electrical conductor opposes a change of the electrical current through it and is defined by

$$V = L\frac{\partial I}{\partial t}. \tag{2.22}$$

This equation can be applied to the Josephson relations to calculate the Josephson inductance L_J. First Eq. 2.18 is used to calculate $\frac{\partial I_J}{\partial t}$. This expression is then used together with Eq. 2.19 to solve Eq. 2.22 for the Josephson inductance,

$$L_J = \frac{V_J}{\frac{\partial I_J}{\partial t}} = \frac{\Phi_0 \frac{\partial\Delta\phi}{\partial t}}{2\pi I_c \cos(\Delta\phi)\frac{\partial\Delta\phi}{\partial t}} = \frac{\Phi_0}{2\pi I_c \cos(\Delta\phi)} \tag{2.23}$$

Using the trigonometric identity and Eq. 2.18 the Josephson inductance can be rewritten as

$$L_J = \frac{\Phi_0}{2\pi I_c\sqrt{1-\sin^2\Delta\phi)}} = \frac{\Phi_0}{2\pi I_c\sqrt{1-(\frac{I_J}{I_c})^2)}}. \tag{2.24}$$

It is easy to see that L_J diverges as the current approaches the critical current or as the phase difference between the superconducting parts of the junction becomes $\pm\frac{1}{2}\pi$. This makes the inductance non-linear, which is necessary for parametric amplification (explained in the next section). Furthermore, if $I_J \approx 0$ the Josephson inductance becomes almost constant

$$L_{J0} = \frac{\Phi_0}{2\pi I_c}. \tag{2.25}$$

where L_{J0} is called the linear inductance of the junction.

2.3.3. SQUID

Two Josephson junctions connected in parallel by superconducting leads form a SQUID (Superconducting QUantum Interference Device)[[18]]. Applying a magnetic field flux to the superconducting loop will affect the phase of the two JJs, effectively modulating the total supercurrent through the SQUID. The total supercurrent through the SQUID will now be the sum of the currents through each junction [38]

$$I_{sq} = I_{c,1}\sin\Delta\phi_1 + I_{c,2}\sin\Delta\phi_2. \tag{2.26}$$

where $I_{c,n}$ and $\Delta\phi_n$ are respectively the critical current and the phase difference between the superconducting parts of one junction. The critical current of the SQUID, under the assumption of identical junctions (symmetric SQUID) and a small signal limit ($\Delta\phi_1 - \Delta\phi_2 \ll \pi$), can be expressed as

$$I_{sq} = 2I_c\left|\cos\left(\pi\frac{\Phi_{ext}}{\Phi_0}\right)\right| \tag{2.27}$$

where the external magnetic flux that passes through the SQUID area enclosed by the superconducting leads is denoted with Φ_{ext}. In the case of asymmetric junctions, this equation becomes more complicated but throughout this thesis, the focus is put on designing and fabricating symmetrical SQUIDS. So, in contrast to the single JJ with a constant L_{J0} for low currents and temperature, the SQUID has an inductance dependent on a tunable magnetic field Φ_{ext}, given by [38]

$$L_{sq} = \frac{L_{J0}}{2\cos\left(\pi\frac{\Phi_{ext}}{\Phi_0}\right)} \tag{2.28}$$

with L_{J0} being the linear JJ inductance Eq. 2.25. When the SQUID is combined with a lumped element LC resonator a tunable resonance frequency given with

$$\omega_0 = \frac{1}{\sqrt{C_r(L_{sq}+L_r)}} \tag{2.29}$$

which basically is a combination of Eq. 2.2 and Eq. 2.28. The resonators' capacitance and inductance are given with C_r and L_r. Based upon this equation a plot can be made (Fig. 2.11) demonstrating what a SQUID measurement should look like if the frequency is measured with a varying external magnetic field.

The fact that the resonance frequency is changing due to the external magnetic flux indicates that the system is tunable for the critical current and Josephson inductance. It is also imported to take into account the loop inductance when designing a SQUID due to the large kinetic inductance of the thin NbTiN layer [35]. The SQUID has a characteristic parameter known as the screening parameter given with

$$\beta_L = \frac{2I_cL_{loop}}{\Phi_0} \tag{2.30}$$

where L_{loop} is the inductance of the loop [20]. When $\beta_L > 1$, the SQUID behavior becomes hysteretic with the external magnetic field which is an unwanted effect. The frequency as a function of a magnetic flux plot would exhibit discontinuous jumps as the magnetic field goes up, occurring periodically with a period of $2\Phi_0$ [20]. So to conclude this section, the JJ (or SQUID) can be understood as a lossless, non-linear element. Because of these properties, the Josephson junction found its way to become the center-piece of a wide range of quantum related applications, such as sensing, quantum information and quantum-limited parametric amplification.

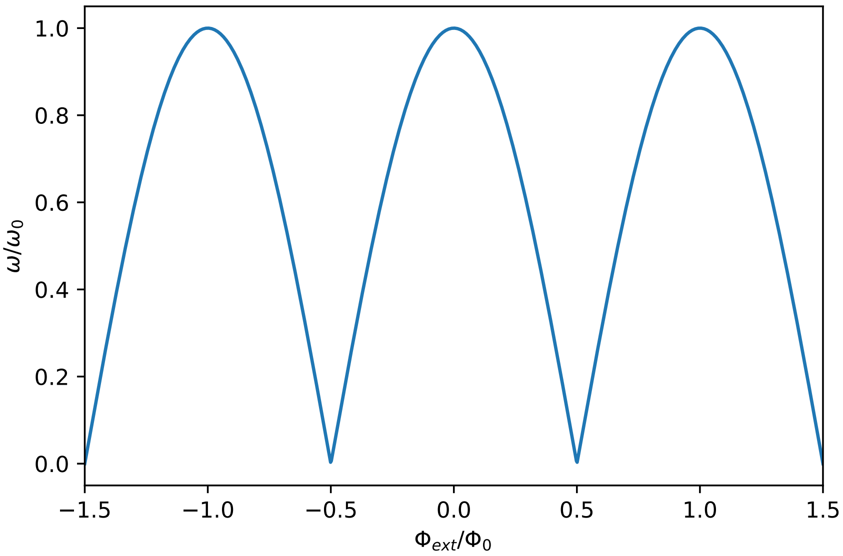

Figure 2.11: The resonance frequency of the JPA is plotted as function of the external magnetic flux. The resonance is periodic and diverges at $\Phi_{ext} = (n + \frac{1}{2})\Phi_0$ with n being an integer number.

2.4. Josephson parametric amplifier

The Josephson junction can provide the nonlinearity needed for a parametric amplification process. When the junction is driven with a strong pump the Josephson inductance is modulated non linearly. To use this nonlinear modulation of L_J the junction is embedded in an LC resonator. The physics behind the operation of the JPA will not be cover in this thesis but the interested reader could read the following references [17], [39] and [6]. The first JPA was demonstrated in 1975 [12]. Since then it has been investigated continuously and many different JPAs are been developed. See Fig. 2.12 for a general overview of different JPA designs.

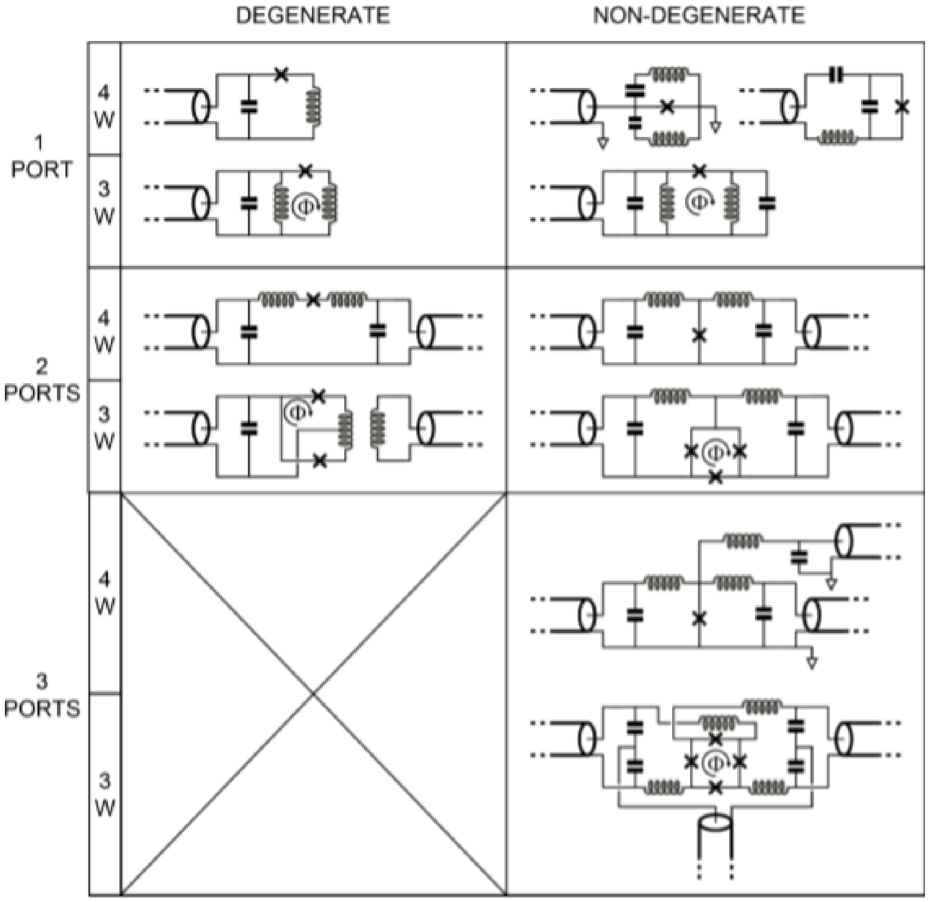

Figure 2.12: Table with various JPAs circuit diagrams. The circuits are classified according to the degenerate/non-degenerate, three-wave mixing/ four-wave mixing and by the number of ports through which the signal, idler and the pump waves are delivered. Image reproduced from [36].

Flux penetrating a SQUID loop is denoted in Fig. 2.12 by the Φ with an arrow circled around it. Instead of current pumping the system with twice the natural frequency, it is also possible to vary the magnetic flux penetrating the SQUID loop which controls the Josephson inductance (Eq. 2.28). This type of pumping is usually for three-wave mixing processes [1]. The SQUID can additionally be used to tune the centre-frequency of the JPA for both three-wave and four-wave mixing processes. However, change in the static magnetic field is very slow which is not practical for multiplexing qubit readout. Researchers are therefore more interested in the bandwidth that can be amplified simultaneously. For the JPA there is a gain-bandwidth constraint caused by the fundamental JPA design itself that forces the user to choose between a high gain in a narrow BW or low gain in a wider BW [4]. This constraint is caused by the coupled LC resonant based circuit. Most of the JPAs operated at 20 dB gain with a bandwidth of 10 MHz. Also, a JPA features a limited saturation power, due to the few JJs in the circuit. The saturation power sets the maximum signal power that can have linear gain. So the signal power where the maximum gain decreases by 1 dB is known as the saturation power or the 1 dB compression point. This is typically 5-10 % of the critical current or -130 dBm [39].

2.5. Traveling wave parametric amplifier

JPAs are used in resonator configurations however, it is possible to lengthen the electric path to be a long nonlinear transmission line. This has to be accompanied with a low-dissipation medium which can sustain the nonlinearity for a reasonable length. It can therefore have a much larger bandwidth while also having high gain. This is the essence of Traveling wave parametric amplification (TWPA) which was theorized back in 1958 [9]. Because the TWPA is not based on a resonant cavity, it is not limited by the gain-bandwidth constraint.

2.5.1. Josephson traveling wave parametric amplifier

Recently a technology called Josephson traveling wave parametric amplification (JTWPA) [25] has been studied. In the case of these amplifiers, the nonlinearity comes from the Josephson junction based transmission line. For every junction in the system, a corresponding shunt capacitor needs to be added to impedance match the 50 Ω transmission environment. Due to the use of many identical junctions (typically between 450-2500 JJs), instead of a few in the JPA, the JTWPA allows the use of high saturation power (≤ -100 dBm). However, using a strong pump causes changes in phase velocities of the propagating waves preventing linear gain performance [30]. By adding capacitively coupled parallel LC resonators into the transmission line, called resonant phase matching (RPM) units, high gain in a broad bandwidth can be achieved (see supplemental material in [30] for derivation). These RMPs also create a stopband in the gain curve because of their resonant frequencies. Signals with frequencies inside of this stopband can not be amplified. Therefore a small spread in RPMs is favorable to minimize this stopband bandwidth. The pump frequency should be close to this stopband to optimize the amplified region as the signal and idler frequencies are symmetrical around the pump frequency for non-degenerate four-wave mixing (according to table 2.1). The JTWPA can in theory reach a gain of 20 dB, an instantaneous bandwidth of 3 GHz and a saturation power of -98 dBm [30]. dBm (decibel-milliwatts) is a unit of level used to indicate that a power ratio is expressed in decibels (dB) with reference to one milliwatt (mW). The same equivalent expressions as for dB may be used but instead of using the ratio between the in and output power the power devided by 1 mW is used, so $10\log(P/1\text{ mW})$. The ability to amplify several signals at different frequencies simultaneously makes the JTWPA another key component for the construction of a large-scale quantum computer. The JTWPA produces a high gain with a wide bandwidth used for qubit multiplexing. A non-degenerate process is needed for this. Both the power and phase of the qubits are important hence a phase insensitive process is needed. We will strive to obtain the same results as in this paper [25] but with a different fabrication method.

3

Methods

This chapter will be an elaborate discussion on the design, fabrication and measurements of the JJs, LC resonators, JPAs and JTWPAs introduced in the theory chapter.

3.1. Design

This section explains the designs created in this thesis. There are in total of six different designs. First, the single JJs and JJ arrays will be introduced. After this, the capacitors and resonator design will be explained. Lastly, JPA and JTWPA designs are discussed.

3.1.1. Josephson junctions and arrays

Josephson junctions are the only true nano-structures in the devices made in this thesis, therefore they are the most critical. There are many types of JJs but in general, they are all just two superconductors being weakly connected. The interesting JJs for this type of devices are the ones based on aluminum oxide (AlOx) as the barrier (weak connection) between the two superconductors (aluminum electrodes). Aluminum is commonly used for these junctions because it oxidizes into aluminum oxide, which forms a suitably isolating thin layer. There are several different methods for fabricating this type of JJs such as the Dolan bridge method [45] and the Nb/Al-AlOx/Nb trilayer method [41] but the method used in this thesis is known as the bridgeless method which creates the "Manhattan Style" junctions or cross junctions. Developed features are designed to be deeper than their width to allow the metal to reach the substrate when evaporated parallel to a given channel, but block metal in orthogonal channels. Thermal oxidation of layer 1 occurs before rotating the substrate and depositing layer 2. [24], see Fig. 3.1.

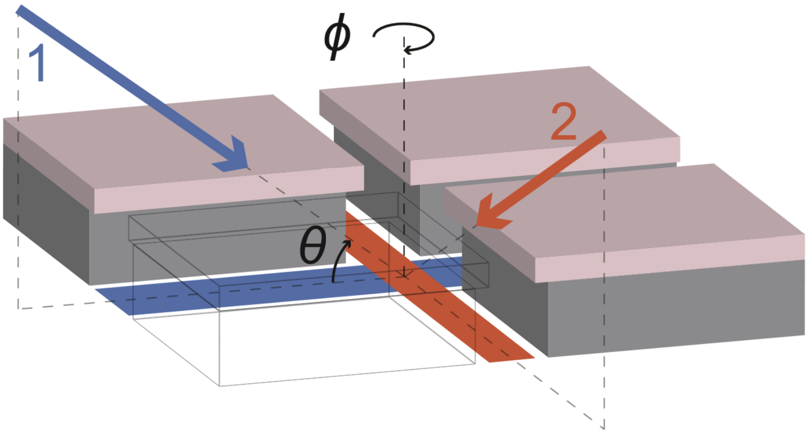

Figure 3.1: The resist stack for "Manhattan Style" junctions.

The bridgeless as well as the bridge method both rely on the principle of double-angle evaporation with a shadow. However, the bridgeless method has some advantages compared to the bridge method:

- The junction area is independent of resist thickness. Relatively large junctions can be made without risking bridges to collapse.
- Reduced aluminum on the substrate. With the bridge method, there are always two spurious junctions fabricated next to the original JJ, this can be prevented with the cross junctions.
- Improved interface preparation. As there is no bridge, more intensively cleaning methods can be applied during fabrication.
- The alignment is less strict when doing the lithography.

The first advantage is actually the most important one for this thesis. The cross junction area depends on the width of the gap exposed inside of the bilayer of resist and on the two angles of evaporation. By using a sufficient thick enough bilayer the designer could make huge junctions. This is the limiting factor for the bridge method where there is a bridge (made out of resist) that can collapse. The bridge method is fine for small junction areas (typically used for transmon qubits) but not for larger ones. This flexibility in designing allows the fabrication of large junction areas which is desirable in the case of the JPA and JTWPA. The goal is to fabricate amplifiers that are able to amplify relative large signals, as they need to support the input signal and the pump signal. Therefore JJs with large critical currents are needed. According to Eq. (2.21) the normal state resistance (R_n) is should be small which is inversely proportional to the JJ area. In the actual design [3.2] a sweep of JJs with different overlap areas is included. Based on these measurements, long arrays of JJs are designed [3.2] to extract more measurement data on those JJs to check their stability around 4.6 μA. $I_c = 4.6\ \mu$A is the target which is based on characteristic line impedance considerations supported by the literature [25]. This critical current should be able to handle high input signals without losing any gain, hence having high saturation power.

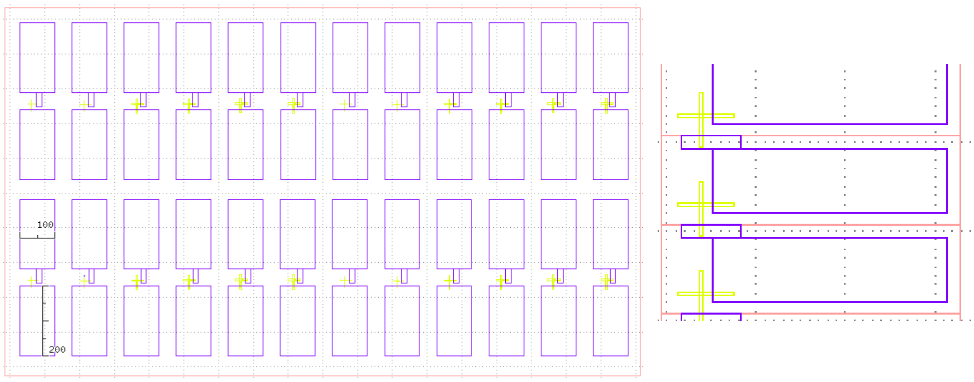

Figure 3.2: Sweeping a range between 1 and 6 μm JJ widths, with a step of 1 μm (left). The probe area (explained more in the measurements section) which is indicated with a ruler is 100x200 μm^2. Three JJs in series which is a small part of a thousand JJ long array (right). The red lines indicated where the silicon base layer is, blue lines show the NbTiN layer and the yellow lines show where the JJ should be fabricated (color online).

3.1.2. Simulating a LC resonator coupled to a transmission line

In this thesis, SONNET is used to get a feeling of what the dimensions should look like for the CPW and resonators. SONNET is a high frequency electromagnetic analysis tool commonly used in this field of research. We will first explain how the transmission line is simulated after this the resonators are explained. For simulating an LC resonator first a resonant frequency has to be targeted. Depending on material choice and fabrication limits a design close to reality can be made and simulated. From this simulation, the expected resonant frequencies and Q factors can be modeled.

Impedance matched transmission line

As discussed in the theory, Matlab is used to find the optimal geometry for the CPW. All cabling in the setup must have the same impedance, otherwise, reflections occur (section 2.2.5). 50 Ω is an industrial standard, dating from the 1930s, which is a compromise between power handling (E field breakdown) and attenuation

Figure 3.3: Top view of the model CPW (left) and a 3D view of the same model (right). The red surface represent the NbTiN, above it there is vacuum and beneath the NbTiN there silicon.

per unit length. By plotting Z_0 (Eq. 2.11), against k (Eq. 2.15) one can select a k which is the closest to Z_0 = 50 Ω. With k we can start creating a geometry in SONNET.

After setting the following parameters

- Dielectric constant silicon = 11.44
- Kinetic inductance of the NbTiN film used in this research per unit square = 0.84 pH/sq
- Thickness Si = 525 μm
- Thickness NbTiN = 100 nm

two ports are added at each end of the central line of the CPW. After this, a symmetric dimension parameter (Wline) is added so that we can find the right simulation result as a function of a geometrical parameter.

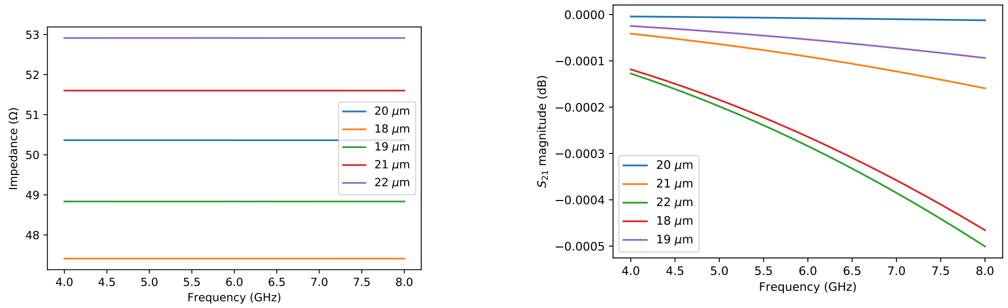

Figure 3.4: Both graphs are plotted with a ABS (Adaptive Bandwidth Sweep) between 4-8GHz. The lines represent different values of Wlines. The port impedance for the different values (left). The transmission from port 1 to port 2 (S_{21}) (right).

In the first figure we see a SONNET graph with the port impedance for different values of Wlines and in the second graph the transmission S_{21} (in dB) for the same parameters. With the parametric sweep of Wline the center conductor (S) of the CPW was fixed and only the gap that separates it with the rest of the film (W) was changed, see Fig. 2.10. We can now see that Wline = 20 μm matches the best the 50 Ω requirement. When Wline = 20 μm the least reflection in transmission is observed, shown in the second figure.

Designing a LC resonator

In both JPA and JTWPA designs an LC resonator is of great importance. For the JPA the LC resonator is used as a resonant cavity in which linear gain can be observed and in the JTWPA design over 100 resonators are used as RPM units. The first thing to do is to select a resonant frequency when designing a resonator. The RPM resonators built in this paper [25] has an inductance of 120 pH and capacitance of 6 pF. However, we chose a different ratio between capacitor (5.3 pF) and inductor (130 pH) as this was more convenient for the design. Using the formula for the electrical resonance frequency

$$f = \frac{1}{2\pi\sqrt{LC}} \tag{3.1}$$

we find a resonant frequency 6 GHz. Which is a smart choice for the JTWPAs as it is in the middle of the 4-8 GHz "sweet spot". In this band is the readout response the strongest and the electronics to support the setup are affordable. The size of the resonators that correspond with this frequency is also compact enough. So the resonator design of this thesis is chosen to be resonant at this frequency.

The next step is to choose what kind of capacitor we want to use. There are two options, the parallel-plate capacitor and the interdigitated finger capacitor. Both capacitors would work, but the finger capacitor is known to have less loss. Nevertheless, we chose to go with the parallel-plate capacitors because finger capacitor resonators are between 10 and 100 times bigger than the parallel-plate alternatives with the same capacitance. For the parallel-plate capacitor, we will use a 100 nm thick aSi:H (amorphous silicon hydrogenated) layer as a dielectric. This is chosen to be the dielectric with the lowest loss [27] for which we also have a PECVD tool capable of depositing such material at the Kavli nano lab (more detailed explanation follows in the fabrication section 3.2.2). We use the well known parallel-plate approximation formula

$$C = \frac{\epsilon_d \epsilon_0 A}{d} \tag{3.2}$$

to design the capacitor of the resonator. In this formula is ϵ_d the dielectric constant, A the area and d the distance between the two conducting plates. Keeping the parameters of the CPW simulation the same we started changing the design. By adding a parallel-plate capacitor followed by a meander a resonance frequency of 6 Ghz was aimed to be achieved.

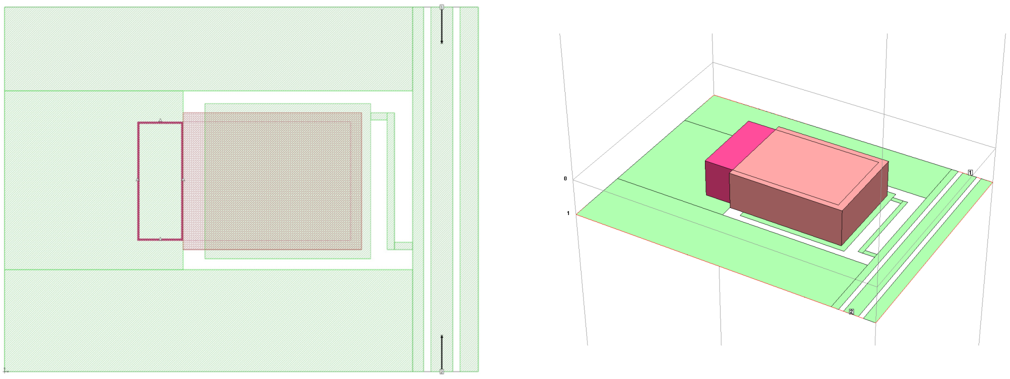

Figure 3.5: The green surface represents the NbTiN, the light pink part is the aSi:H dielectric brick and the dark pink part is a thin aluminum layer partially on top of the brick and a via at the left side which allows the top electrode of the capacitor to ground. Top view of the model LC resonator (left) and 3D side view (right). Again with vacuum above the NbTiN and beneath it there is 525 μm silicon.

Resonance frequency and Q factor

The design as modeled is an LC resonator coupled to the CPW feedline (simulated before). By changing the geometry of the resonator we try to target the resonant frequency at 6 GHz.

The graph shows the minimum transmission at resonance frequency $S_{21,min}$ which is 6.23175 GHz. The actual fabricated resonators, JPAs and RPMs in the JTWPA are measurable as long as they have resonant frequencies in the 4-8 GHz window. In addition to finding the resonant frequency, the graph can also be used to determine the Q factor with

$$Q_{tot} = \frac{f}{BW} \tag{3.3}$$

where f is the resonant frequency and BW is the bandwidth, both in Hz. The BW can be obtained by measuring the frequency difference at the half-power point, given with the following expression [26]

$$S_{21,BW} = 10\log\left(\frac{1+S_{21,min}^2}{2}\right). \tag{3.4}$$

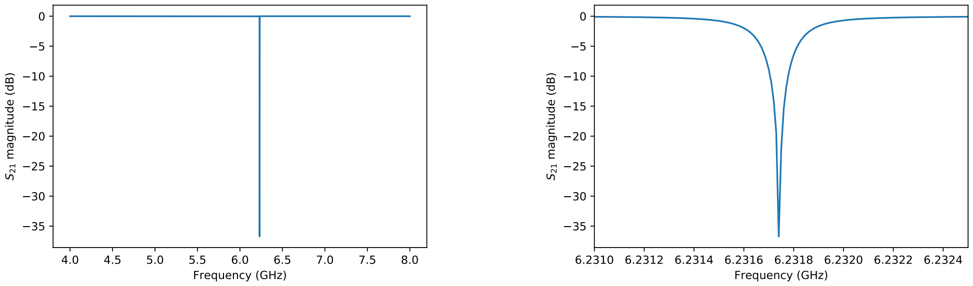

Figure 3.6: After simulation the transmission (S_{21}) is plotted. The dip in frequency is where the resonance frequency is. The left graph show the plot with a ABS of 4-8 GHz and the right plot is a zoom in of the same plot.

From the simulation we observed an under coupled resonance dip at 6.23 GHz. The dip is very deep because we did not include any loss in the dielectric. The dielectric loss and the internal Q factor are related with the give formula

$$\tan\delta = \frac{1}{Q_{int}}. \tag{3.5}$$

This indicates what the dielectric loss is in the capacitor due to the dissipation of electromagnetic energy.

3.1.3. Parallel-plate capacitors and LC resonators

The LC-resonator designs in this thesis are based upon the dimensions of the SONNET simulations

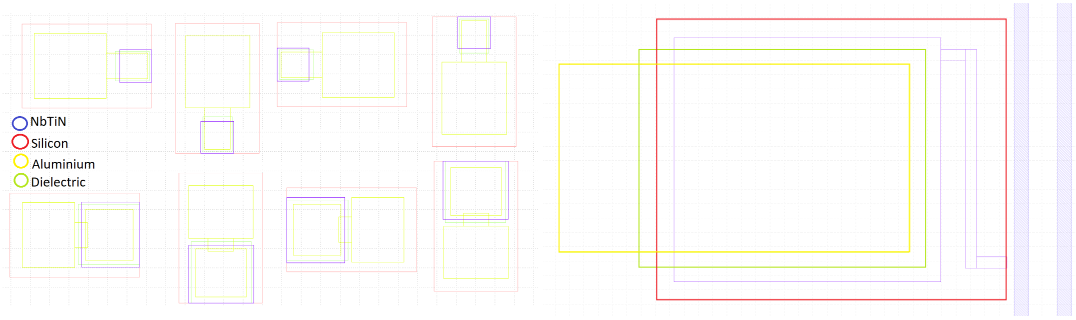

Figure 3.7: Capacitors with different orientations, with corresponding legend for the colors(left) and resonator design (right).

The aluminum is not only used as the top electrode of the capacitors, but also for the cross-junctions used in the JPA and JTWPA. This means that the angle of evaporation plays an important role in the design. To ensure the correct orientation on which the capacitors are made, we designed four capacitors, each with its own direction, as shown in Fig. 3.7. With these test capacitors, we could easily probe the top plate to check which orientation is connected to ground (short).

3.1.4. JPA

For the JPA design, we adapted the resonator design to make the JPA more capacitively coupled to the feedline and we added a SQUID loop at the end of the inductor.

When the JPA circuit diagram is compared with the circuits in Fig. 2.12, it can be seen that it closely matches 1 port four-wave mixing JPAs (top row). There are two important factors when designing the SQUID.

- First, we have to take into account that the critical current of the SQUID which is a summation of the critical currents of the JJs Eq. 2.26. So, if one wants to keep the same critical current, the overlap area of each JJ has been halved.

- Second, to prevent hysteretic behavior the size of its loop needs to be as small as possible according to Eq. 2.28. For this design we found β_L to be $\ll 1$, using a convenient conversion factor for the self-inductance of wire per unit length ($1cm = 1nH$) and the length found in Fig. 3.9 which is 20 μm for the loop.

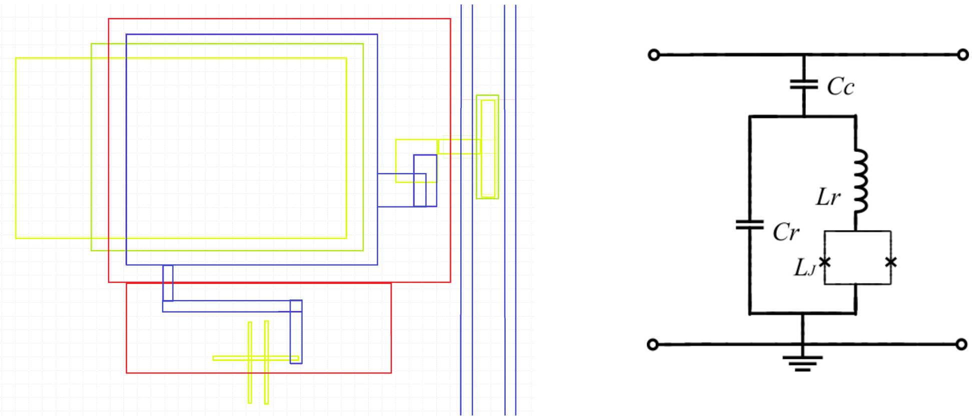

Figure 3.8: Design of the JPA (left). We kept the inductance and capacitance the same as the resonator by having the same parallel-plate capacitor area and the same meander coil length for the planar inductor. Circuit diagram of the JPA (right). The two crosses represent the JJs which form the SQUID.

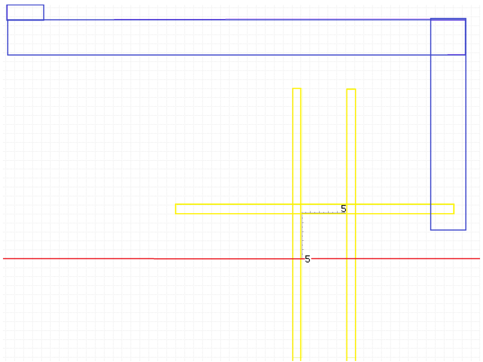

Figure 3.9: Zoomin of the SQUID loop in the JPA design. The meander coil inductor ends on top and the SQUID is formed with two Josephson junctions. The dimensions of the loop are indicated to be 5 μm each side.

Knowing the loop area of the SQUID (=25 μm^2) the expected periodicity of the JPA resonance frequency (depicted in Fig. 2.11) can be found using the following basic formula

$$\Phi_0 = B \cdot A \tag{3.6}$$

where B is the external magnetic field, Φ_0 is the magnetic flux quanta and A is the area.

3.1.5. JTWPA

There are in theory two JTWPA designs which work with different pump processes; flux [47] and current pumping [30]. Flux pumped JTWPAs are based on SQUIDs instead of single JJs. This type of TWPA is therefore referred to as a SQUID traveling-wave parametric amplifier (STWPA) [28]. By using a magnetic field it is possible to flux pump the STWPA in a three-wave mixing process [46]. Therefore, no RPM unit is needed as the two signal do not travel together in the same path. The phase can be independently engineered. Additionally, this allows the STWPA to tune the Josephson inductance of the SQUID which will change the characteristic impedance of the transmission line to have a perfect impedance match with the rest of the system. However, the current pumped JTWPA has been studied more which ends up having a better gain and bandwidth performance [25]. An advantage for the JTWPA is that the device is not sensitive to magnetic field fluctuations and so a high degree of magnetic shielding is not necessary. The structure of the current pumped JTWPA is basically a long chain of unit cells. The unit cell consists of n number of Josephson junctions (L_r) each with its own shunt capacitor (C_s) followed by a capacitively coupled (C_c) RPM unit (C_r and L_r) [1].

In the case of this paper [25], one unit cell consists of three Josephson junctions and one RPM unit resonator. The value of the third shunt capacitor is reduced to compensate for the addition of the couple capacitance (c_c) of the RPM. In our case, we chose to use three JJs per unit cell (just like [25]) but other configurations

---

[1] The background of the design snapshot is black colored as it is taken from different designing software

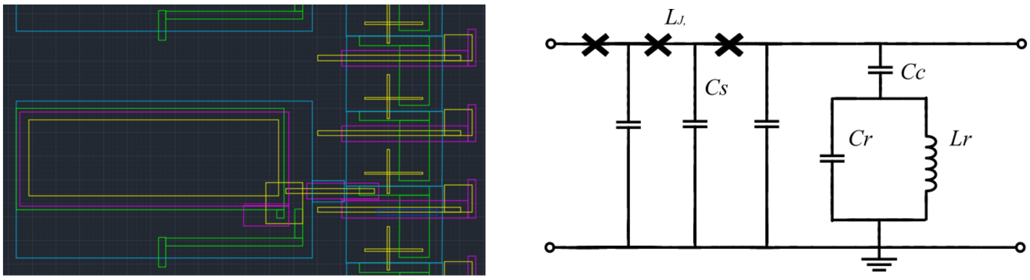

Figure 3.10: The JTWPA design for this thesis (left). Green color is the NbTiN pattern, yellow is Al, blue is Si and purple is the dielectric. The inductance and capacitance are kept the same as the resonator. The circuit diagram of one unit cell of the JTWPA (right).

have been tried before [44].

3.2. Fabrication

This section will be an elaborate description of the processes used to fabricate the devices. Typical dimensions are micrometers (μm) in the plane of the wafer and range from a few nanometers to hundreds of nanometers (nm) for the vertical dimensions, hence we talk about nanofabrication. The explanation of the fabrication techniques will be limited to the ones used in the thesis. For more information, the reader is referred to the textbook [14]. The section is divided into three subsections each for every lithography step. All processes discussed are done in the Kavli Nanolab in Delft.

3.2.1. First lithography step

In this lithography step, the base layer of the chip is defined. We will cover the choice of material and the relevant tools used to deposit and pattern.

Preparation for first deposition

Every device built in this thesis started off with a Topsil silicon wafer. The surface of Si contains a native oxide layer which in our case is removed with a buffered oxide etch (BOE) which is a wet etch process. It is a mixture of ammonium fluoride (NH4F) and hydrofluoric acid (HF). Hydrofluoric is a solution of hydrogen fluoride (HF) in water. The BOE is diluted with water (1:1). After the wet etch the wafer undergoes a HMDS (Hexamethyl disilazane vapor) treatment to make the surface hydrophobic which increases the adhesion of the deposited film.

NbTiN sputtering

As a superconducting thin film base layer of our chips, we chose to sputter NbTiN. This is often used in superconducting devices, as it is magnetically stable, to minimize resistive losses. There are two main techniques to deposit NbTiN on a substrate, Atomic Layer Deposition (ALD) and sputtering. We chose for sputtering which is a physical vapor deposition (PVD) method where a target (in this case NbTi) is bombarded with Argon ions (Ar^{+}) such that it ejects Nb and Ti particles. Also, nitrogen gas is added to the vacuum chamber as a reactive component. The particles which are ejected from the target will subsequently condense on the wafer substrate due to an applied bias voltage and the nitrogen gas, forming a thin layer of NbTiN. This is referred to as reactive sputtering because of the use of a reactive component. After deposition, this layer is measured with a four-point probe measurement to get the sheet resistance needed for calculating the kinetic inductance per unit square ($L_{k,s}$). This $L_{k,s}$ typically varies 10% across a 4-inch wafer. This can be improved by the use of ALD [40]. However, we did not use it as the deposition rate is rather slow (typically a few hours) as for sputtering it took 4 minutes to reach a 100 nm thin film. Also ALD tends to give lossy material while sputtering results to have better conductivity.

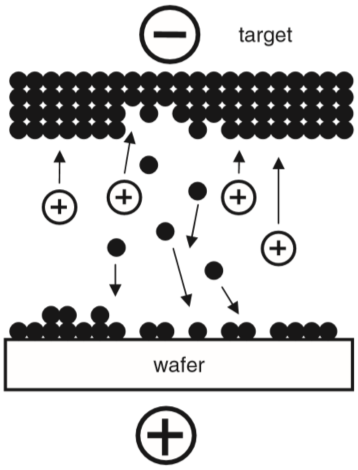

Figure 3.11: Schematic of a sputtering system taken from the textbook [14]. In general, Ar^{+} ions knock atoms out of a target. The knocked-out atoms travel in the vacuum chamber and deposit on the Si wafer. In reactive sputtering, there is also a reactive gas present in the chamber which enhances the deposition process.

It is important to note that there will always be some argon trapped in a sputter film, but its effect can usually be neglected, because argon is a noble gas and therefore non-reactive. Incorporation of residual oxygen or nitrogen is much more pronounced, because they are reactive and form oxides and nitrides. After the reactive sputtering another thin film deposition process is done to deposition a 100 nm oxide layer as protection for the wet etch which will be included in a later fabrication round. The first fabrication cycle in which we only made LC resonators, capacitors and single JJs was with a NbTiN layer, only because we did not use a wet etch.

Electron beam lithography on NbTiN tiles

After sputtering, the wafer is diced into about 20 tiles of 2 by 3 cm which are easier to handle during fabrication. Before dicing we cover the wafer with a dicing resist (S1805) to protect the film from scratches. The fabrication process so far was performed only once at the start of the thesis. Every new fabrication round started usually with four of these tiles, or samples, with dicing resist on top. To dissolve resist layer the samples are cleaned with hot (53 °C) acetone for 10 min, 5 min ultrasound (power 9) then with hot (86 °C) isopropanol (IPA) for 10 min and finished with 5 min ultrasound (power 9) and IPA rinse. Electron beam lithography is the technique chosen to define the structures on the samples. It is critical to have good adhesion when making micro patterns, so we start first with HMDS. Then a layer of high-contrast positive tone e-beam resist (CSAR 6200.18) is spin-coated onto the sample surface. The spin-coated resist still contains solvent, so a pre-exposure bake of 3 min at 160°C is added to remove most of the solvent. The next step is to expose the designed pattern by an electron beam pattern generator (EBPG) at 100 kV acceleration voltage with a dose of 360 $\mu C/cm^2$. Positive tone photoresist reacts with the electrons coming from the e-beam causing the polymers to break down which can be removed by a developing solvent. As developer pentyl acetate is used which etches the exposed parts of the resist away and as etch stop we use xylene (pre stop) and IPA. In Fig. 3.12 a schematic overview of the different steps is shown.

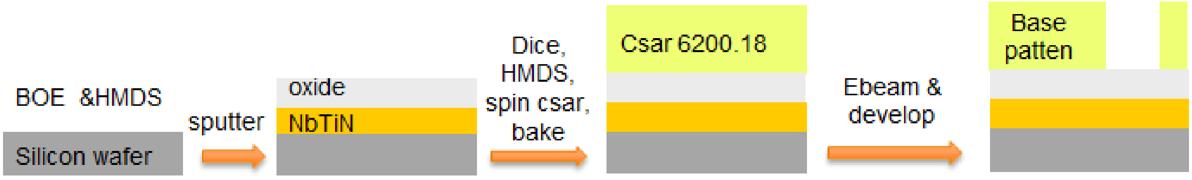

Figure 3.12: Overview of the steps taken to pattern the NbTiN base layer. First, the oxides are removed with BOE. HMDS is added to improve the adhesion of the reactive sputtered NbTiN film. After this film, an oxide film is sputtered on the wafer. Then a resist is spin-coated on the sample. Next, an electron beam exposes the resist to reproduce the designed pattern. Finally, a developer removes the exposed area and leaves the unexposed mask behind.

NbTiN etching

Before we move on to etching we hard bake the developed resist for 1 min at 140°C. This hardens the resist and reduces the selectivity which is useful for the plasma etching as it is an energetic process. During the etch the resist protects the areas where the material needs to remain and open areas are etched. The oxide layer as well as the NbTiN layer is etched with an SF_6/O_2 Reactive Ion Etch (RIE). The Leybold RIE systems consist typically of a cylindrical chamber with two electrodes positioned at the top and bottom. The sample is placed on the bottom plate (positive charged electrode) and gases flow into the vacuum chamber (6 μbar) from the top electrode. An RF source (60 W) generates a fast oscillating electromagnetic field which causes the electrons to strip from the SF_6/O_2 (145/12 sccm) gas molecules, hence creating a plasma. These electrons will eventually charge the sample making it negatively charged. This will attract the ions which will bombard the surface. Together with the chemical reaction of the ions the etch becomes almost anisotropic when defining the base pattern. The way to know when to stop etching is by focusing a laser at the metal and to look at the reflection. The NbTiN reflects more than Si so when there is a change in intensity of the reflected beam we know that the Si is reached. However, checking the sample after the dry etch with an optical microscope we found the Si surface to be contaminated with some residual referred to as "cookie crumbles" see left figure. These defects originate probably from the resist reacting with the plasma or ion bombardment.

To prevent this crumbling effect we decided to do a partial dry etch and finish with a wet etch. Assuming the same time it would take to etch the whole NbTiN from our first dry etch we etched less time, preventing the etch to reach the silicon. For the wet etch we used a bath of ammonia, peroxide and water (1:1:5). The bath is put inside a water bath at 35°C to fasten the etching. The CSAR resist dissolves inside this bath but not the oxide which protects the NbTiN. The wet etch almost has a perfect selectivity which means that the oxide on the NbTiN is not affected by the wet etch. After the wet etch the residual resist that has been damaged or transformed by plasma is stripped off with a hot bath (88°C) of N-Methyl-2-pyrrolidone (NMP) then

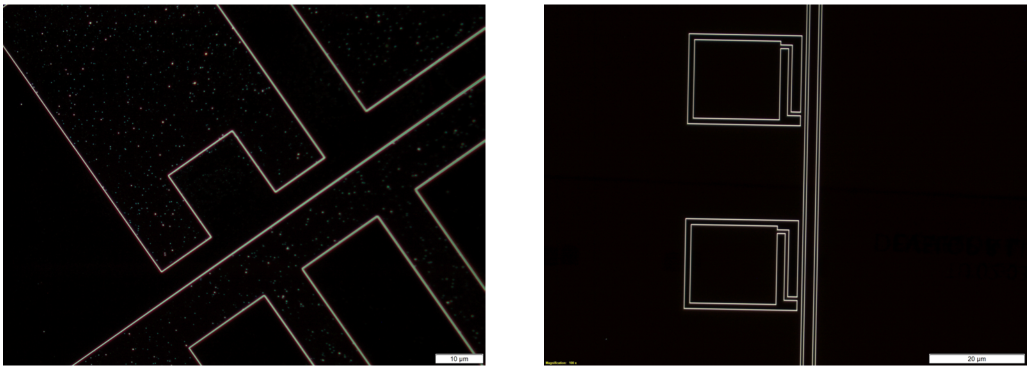

Figure 3.13: Two dark field optical microscope images showing the sample surfaces after etching. Surface with only dry etch (left) and the surface with the combined etch (right).

ultrasound and IPA. See Fig. 3.13 for the improved surface shown in dark field. Fig. 3.14 shows bright field images of the devices made.

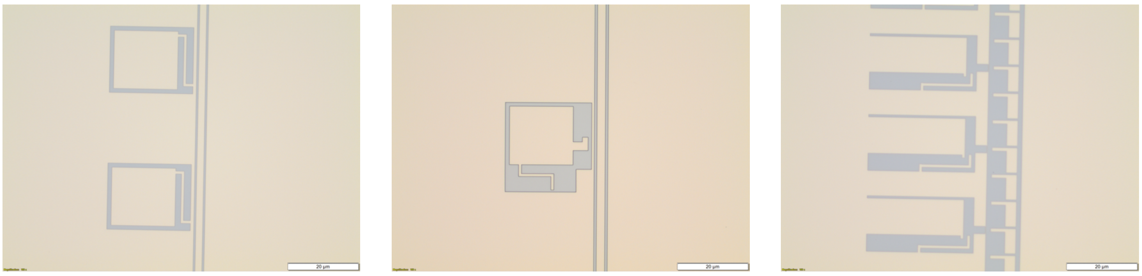

Figure 3.14: The patterned NbTiN base layer of the resonators (right), the JPAs (middle) and the JTWPAs (right).

3.2.2. Second lithography step

This lithography step is dedicated to the dielectrics that form the parallel-plate capacitors. We will cover the choice we made in dielectric and etching process. Note, before depositing the dielectric, diluted HF is used to remove the oxide, used to protect the NbTiN layer from the wet etch.

Deposition of the dielectric layer

As dielectric, we chose hydrogenated amorphous silicon (a-Si:H) which is an amorphous material with embedded hydrogen. This is made with a Plasma Enhanced Chemical Vapor Deposition (PECVD), see Fig. 3.15 for schematic illustration.

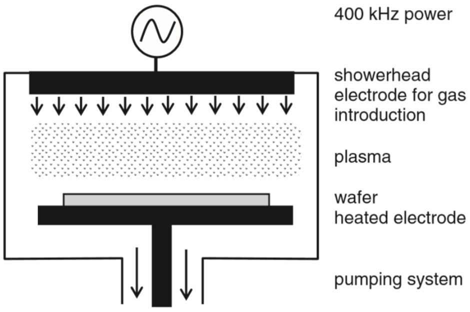

Figure 3.15: Schematic PECVD system taken from [14]. The samples are placed on a heated bottom electrode, the source gases are introduced from the top, and pumped away around the bottom electrode.

Chemical reactions are involved in the process, which occur after creation of a plasma of the reacting gases. With this process we deposited an aSi:H layer with relatively low temperatures which is necessary as we do not want to oxidize the NbTiN [15]. After the deposition, we prepare the samples for electron beam lithography. We reduce the writing time by using a negative tone resist (ARN 7700.18). Negative resists react to the incoming electrons by polymerizing. Test sample structures are made to target the right dosing of the electron beam. The doses varied between 80 $\mu C/cm^2$ and 180 $\mu C/cm^2$. The unexposed portions are removed by using Microposit MF-321 developer. However, the ARN resist needs a post-exposure bake of 2 min at 110°C on the hotplate. This is needed to enhance the bonds in the polymers within the patterned regions.

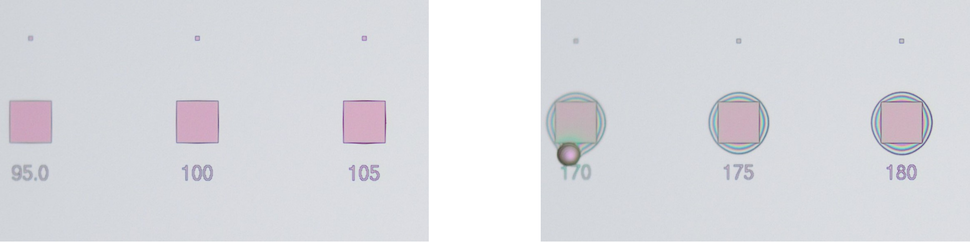

Figure 3.16: Images taken from a optical microscope. The numbers under the pink squares represent the doses in $\mu C/cm^2$. We found 100 $\mu C/cm^2$ to be the right dose (left). The right image shows how the squares look after over exposure.

Choosing the etching process for the dielectrics

Having these test samples with the right dose we proceed with a hard bake of 2 min at 130°C. After the bake, we tried to find a good etch process for the aSi:H. We investigated in two RIE processes, SF_6/He and CHF_3/O_2. Both processes should be anisotropic but they differ in etch rate. The etch rate for CHF_3/O_2 ≈8 nm/min and for SF_6/He ≈50 nm/min. The SF_6/He etches faster and results usually in more anisotropic sidewalls and good selectivity. As for the CHF_3/O_2 we would expect the selectivity to be less as it uses O_2 which is referred to as a "scavenger" [14], it reacts with a lot of chemicals, which is why it is often used in chamber cleaning recipes. The resist is stripped off with a hot (88°C) organic solvent stripper known as J.T. Baker PRS-3000, ultrasound and hot IPA to conclude the stripping for both test samples. After this we studied the test samples under a Scanning Electron Microscope (SEM), see Fig. 3.17.

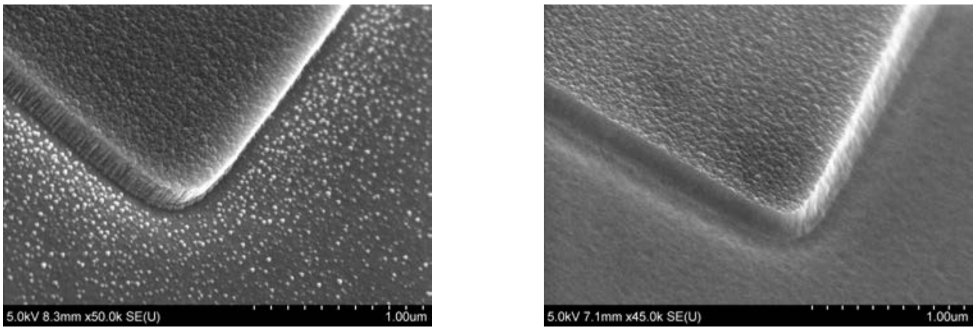

Figure 3.17: Tilted view from a SEM of the two samples. The sample etched with SF_6/He (left) and the sample etched with CHF_3/O_2 (right). Notice the surface rough surface of the SF_6/He etch compaired to the CHF_3/O_2 etch.

The SEM has two advantages compared to the optical microscope. It has a higher magnification (we can see 5 nm details) and a better depth of field (greater focus range). Tilted views reveal information such as the sidewall surface quality of film roughness. The sidewalls seemed indeed more anisotropic for the SF_6/He. However, the SF_6/He etch seems to react with the NbTiN surface. Because of this, we decided to use the CHF_3/O_2 etching process. SF_6/He is the same gas we used to etch the NbTiN in the first lithography step. So it is expected to etch NbTiN. However one could try in future development to increase the helium gas flow as He is known for stabilizing the etch [14]. Fig. 3.18 shows bright field images of the devices made. As the second lithography step is completed we see that the dielectrics of the capacitors are left on the device only where intended. The aSi:H as a light blue color under the optical microscope. Note that it has a transparent property as it is an amorphous material.

Fabrication issues with ALD dielectric devices

Some time has been investigated in fabricating samples with aluminum oxide (Al_2O_3) deposited with ALD. With ALD we can control the thickness atomic layer by atomic layer making the film extremely homogeneous and precise. ALD works in a pulsed mode, see Fig. 3.19.

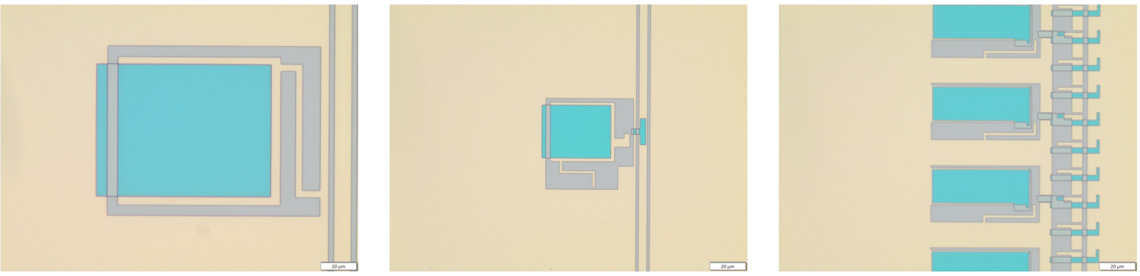

Figure 3.18: The pattern of the resonators (left), the JPAs (middle) and the JTWPAs (right). The JPAs and JTWPAs both use couple capacitor(s) and the JTWPA also has additional shunt capacitors after each JJ.

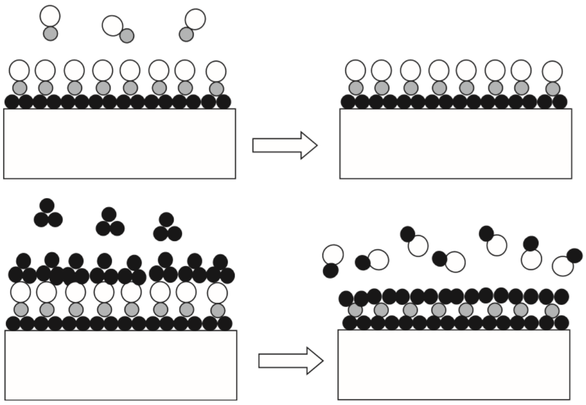

Figure 3.19: Figure illustrating the ALD pulsed process taken from [14]. First chemical bonds are formed between precursor gas molecules and the surface atoms. The second step is to remove the extra precursors with a gas pulse. Thirdly, second precursor gases are pumped into the chamber. They react with the layer deposited in the previous step. Lastly, the reaction products are removed again with a gas pulse and the cycle start all over again.

The growth rate of Al_2O_3 is about 1.1 Å per cycle and the deposition time for a film of 100nm is 3.5 hours. After deposition, we wet etched the Al_2O_3 with a hot bath (66°C) of aluminum etchant type D. The etch rate at this temperature should be 45 nm/min according to the specification properties document from the company Transene. We etched for 4 min to be sure that all the Al_2O_3 is removed. During the inspection, we discovered that the dielectric did not etch completely in some regions, on the left in Fig. 3.20. On the right, in Fig. 3.20, we see the sample after a wet etch of 12.5 min. The Al_2O_3 is still visible which leads us to suspect that the negative resist did not develop well enough, so a bit of resist was left in the narrow spaces.

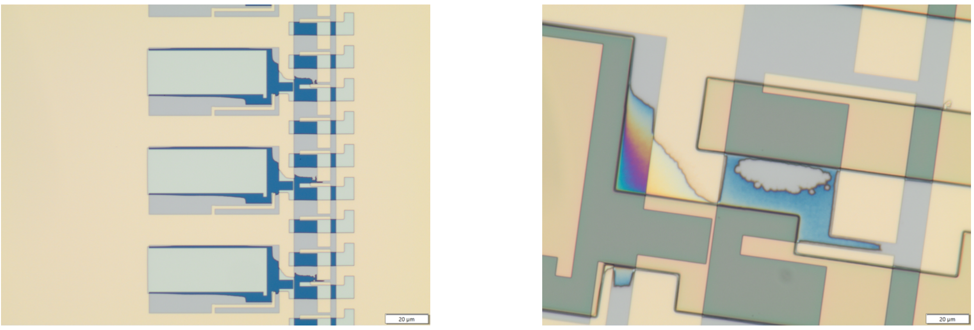

Figure 3.20: Images from the JTWPAs with Al_2O_3 taken from a optical microscope. The defects are repeatedly on the transmission line close to the RPM resonator. Sample after a etch of 4 min (left). We also tested the extreme and etched the sample for 12.5 min (right).

This defect causes problems with the evaporation of the aluminum for the junctions in the third lithography step. The junctions will not be able to contact the NbTiN because of the Al_2O_3. This results in an open circuit, preventing transmission of the microwave through the amplifier. The defect was not present on the LC resonators and JPAs but because our main focus is to fabricate a JTWPA, we did not continue with these samples. We could have stripped the dielectric layer and start the second lithography step again or just fabricated on a new NbTiN tile but there was no time for this in the planning. Fortunately, the aSi:H samples seemed not to suffer from this so we preceded the process.

A possible reason that we did not see these defects in the aSi:H samples is because they were etched with a CHF_3/O_2 plasma. This etch has low selectivity, due to the oxygen plasma in particular, which means that the remaining undeveloped resist is etched away hence opening these narrow areas. This is not the case with the wet etch since this etch has high selectivity.

3.2.3. Third lithography step

The third lithography step is the final step in which we finish the capacitors and fabricate the Josephson junctions using a double-angle evaporation technique and lift-off.

Bilayer spinning and patterning

For the Josephson junctions, we decided to use a bridgeless method [24]. This type of junction has the advantage over Dolan bridge design, that the junction area is independent of resist thickness. The method requires the use of an undercut. Negative resist has an undercut but we used a combination of two positive resists (bilayer) to keep the writing time considerably short. Before spin-coating, the samples underwent a baking of 3 min at 110°C to remove possible absorbed water. We chose copolymer methacrylic acid (MAA) for the first resist layer and the second layer is poly(methyl methacrylate) (PMMA) 950 A11. Note that the small size of the Josephson junctions limits our choice in lithography process. We need the small wavelength of an electron beam to define our structures, wavelengths used with optical lithography would be insufficient. The MAA is more sensitive to the electrons from the EBPG than the PMMA, which results in an undercut. We chose to have a thin undercut to reduce spurious aluminum on the sample hence simplifying the lift-off procedure. After spinning and exposing the resists, we arrive at the development. Initially, we started developing with a mixture of methyl isobutyl ketone (MIBK) and IPA with a ratio of 1:3. After development, the results of the lithography process are checked. We found cracks in the resist, next to the exposed areas, everywhere on the sample, see left Fig. 3.21.

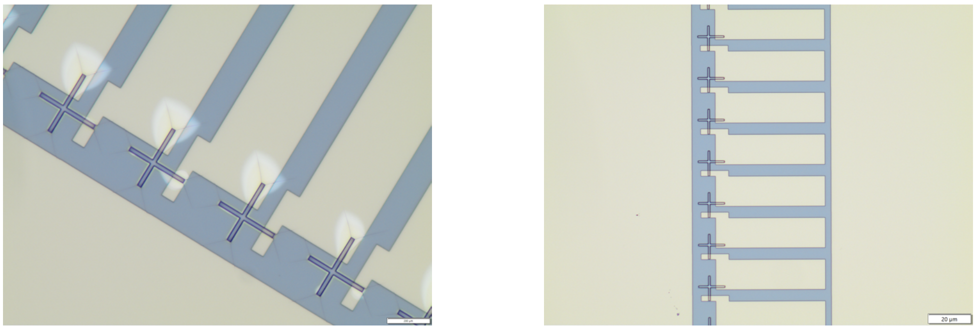

Figure 3.21: Optical microscope images of the JJ array structures taken after development. Sample developed with a mixture of MIBK and IPA (left) and sample developed with a mixture of H_2O and IPA (right). Optical microscope is focused on the top resist for both images.

The areas next to the cracks were measured with a profilometer [14]. When the measurement indicated that the resist layer slowly decreases close to the developed area (grayish area), then the mechanical stylos drops to the silicon substrate. The cracks and grayish areas were randomly sized on the whole sample. Our hypothesis was that the developer degraded the MAA resist too fast causing the top PMMA resist to collapse just enough for the top surface to crack. We decided to use a cold (-15 °C) developer to reduce this fast degrading hence preventing the cracking and decrease in resist height, see Fig 3.21. Even though we have no evidence that this has improved the yield of the devices it is good to have a process that is more reproducible.

Double-angle evaporation method

After development, the samples are cleaned with an oxygen plasma dry etch and a diluted BOE wet etch to ensure good contact of the deposited aluminum and the surface of the samples. The bridgeless JJs require a directional PVD method known as evaporation. Evaporation works by electron beam heating a metal like aluminum (Al). The hot metal atoms turn into a vapor and in high vacuum the vapor will be transported to the substrate which is upside down, right above the heated metal, see Fig. 3.22.

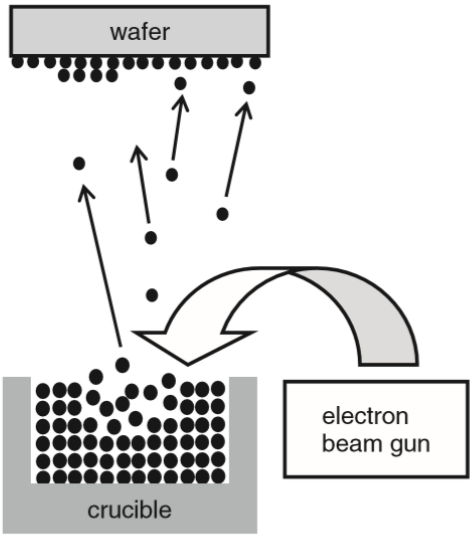

Figure 3.22: Figure from [14] describing PVD evaporation. The electron beam gun heats up the metal in the crucible. The evaporated atoms form a vapor and are transported in high vacuum to the substrate right above the crucible.

The chamber pressure is typically 10^{-7} m Torr, this causes the atoms not to collide with each other and it enhances the film quality (fewer impurities). The bridgeless method combines the directionality of evaporation with a tilted sample creating a shadow, called angle evaporation. To create the JJs we use two angles, so double-angle evaporation.

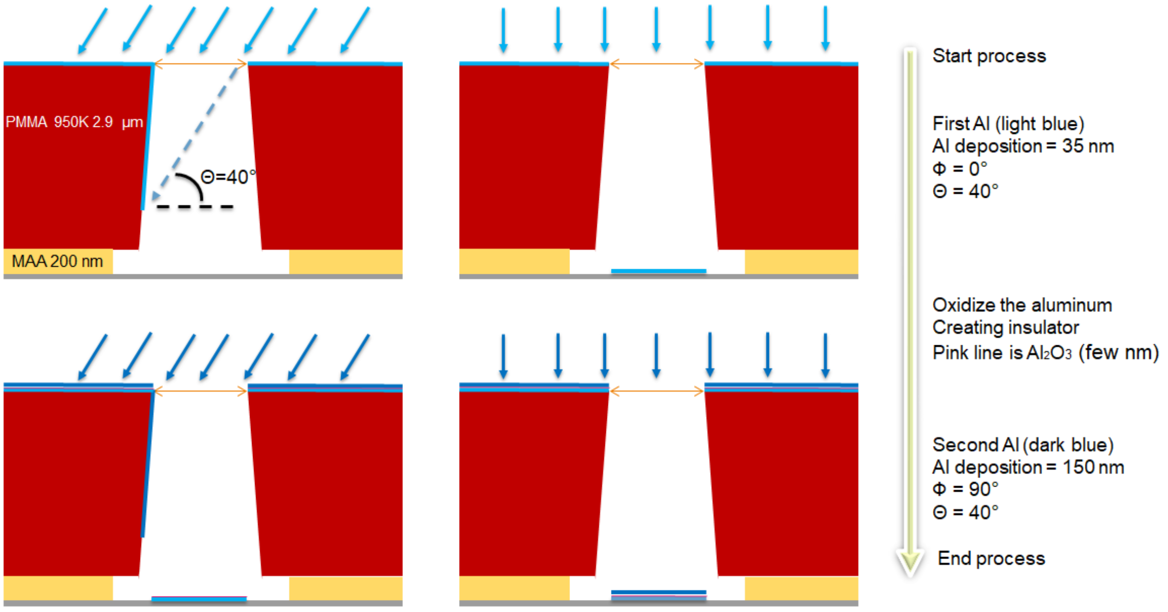

Figure 3.23: The double-angle evaporation method, consistent with Fig. 3.1. The overlap area of the JJs depends on the top opening of the developed resist stack indicated with the orange double sided arrow and the evaporation angle indicated with the light blue arrows.

The samples are aligned on a holder and placed upside down in the high-vacuum chamber. The sample holder is tilted 40 degrees (θ=40°) while the crucible with Al inside is heated up with the electron beam. When the holder is properly aligned above the sufficiently heated Al, a shutter will open and the samples are exposed to the evaporating Al. The particles have a mean free path that is longer than the chamber due to the high vacuum, so they deposit directly on the samples. The rate of evaporation and the amount of metal to be evaporated can be set by the deposition controller. Once the desired amount of Al is evaporated the shutter is closed. The next step is in-situ oxidation of the deposited Al. The holder is also rotated 90 degrees (ϕ=90°)

during oxidation and the tilt remains the same. The shutter then opens again, causing the second deposition to take place. When the desired thickness is reached the shutter is closed. One of the samples was broken so we could inspect the cross-section under an SEM, see Fig. 3.24.

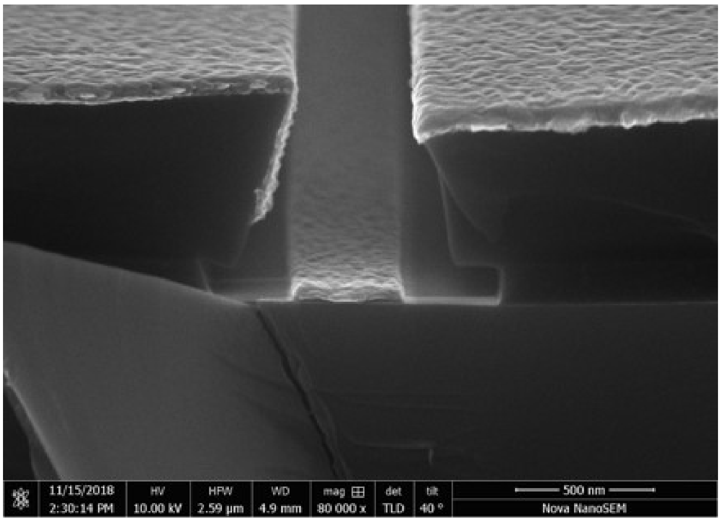

Figure 3.24: A SEM image made from the cross section of a sample after the double evaporation. This image corresponds to the bottom left side sketch of Fig. 3.23.

The top electrode of the capacitors is also fabricated during this step. The capacitors are complete when the Al is deposited on the dielectrics. The shadow plays no role for the resonator capacitors because these areas are typically large. However, the couple capacitors and shunt capacitors (for JTWPA) are smaller, which causes this shadowing effect to become relevant. After the double-angle evaporation, the samples are diced into our final devices. Dicing the samples speeds up the lift-off process. The deposited Al on the samples also acts as an additional shield (under the dicing resist) against stretches that may occur during dicing.

Lift-off

We remove all the metallization (Al deposited), that is not in contact with the substrate, with a solvent that dissolves the resist. This process is known as lift-off, see Fig. 3.25. Lift-off metallization should have poor step coverage, and therefore the method of choice is evaporation. Aluminum deposition with an ALD, CVD or sputtering has a relative good step coverage which will prevent the Al on the resist from lifting off.

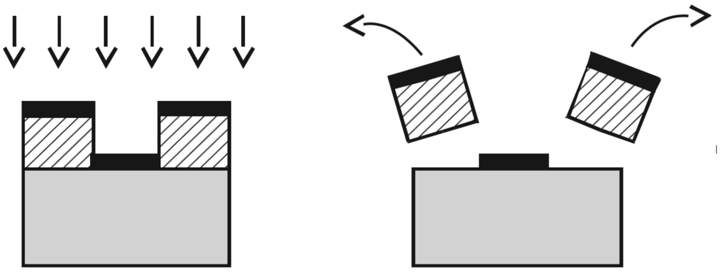

Figure 3.25: Schematic illustration of the lift-off process taken from [14]. Metal deposition on sacrificial resist (left). Resist dissolving causing the metal to lift-off (right). The thickness of the film deposited needs to be less than the resist thickness, in order for lift-off to work.

The samples are diced into our final devices before lift-off. This will reduce the amount of structureless area which decreases the processing time. The lift-off solvent needs to propagate under effectively less area which makes the resist stripping easier. The lift-off solvent suited for dissolving the bilayer of resist is NMP. The NMP is heated to 88°C and the samples are placed inside the bath for 30 min. After 30 min a glass pipette was used to enhance the lift-off process. If there still is unwanted Al, the samples are put in a new NMP bath and the process repeats for another 30 min. The lift-off process concludes with ultrasound and IPA rinse. Fig. 3.26 shows a cross junction before and after lift-off.

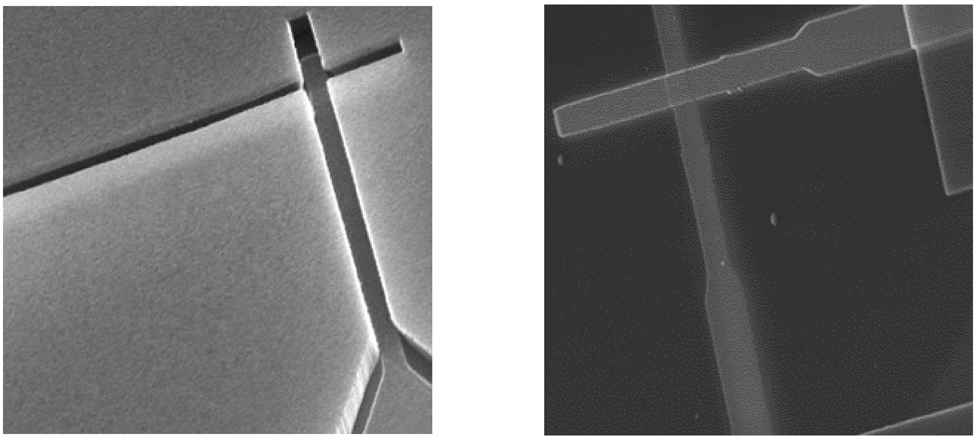

Figure 3.26: Two tilted SEM images of a cross junction, before (left) and after (right) the lift-off. The Josephson junction is formed in the middle where the two Al deposition layers intersect. The first Al deposition comes from the top side and the second from the left side of the image.

3.2.4. Final devices

After our final fabrication run we ended up with 15 JTWPAs on 1 chip (see Fig. 3.30 for full JTWPA picture), 10 JPAs on single chips, 3 single JJ and capacitors test structure chips, 5 long arrays of hundreds of JJs and 2 transmission lines with coupled resonators chips. In Fig. 3.27 we demonstrate three types of devices that we performed the cryogenic measurements on.

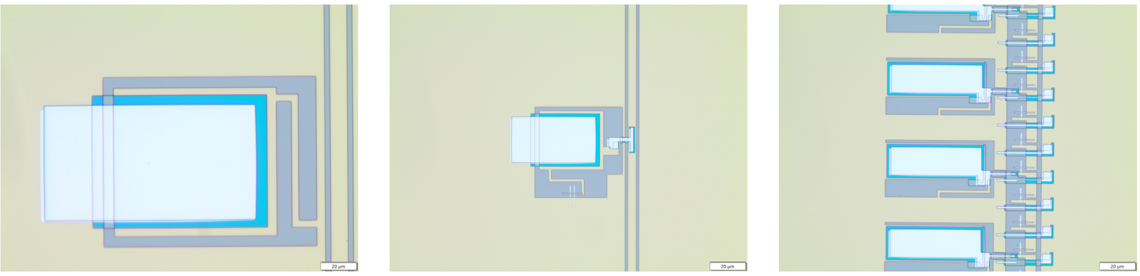

Figure 3.27: Three optical microscope images of the devices fabricated, 1 resonator inductively coupled to a CPW (left), JPA capacitively coupled to a CPW (middle) and at least two unit cells of the JTWPA (right). Note the relative large resonator capacitors and the smaller shunt (for JTWPA) and couple capacitors (for JTWPA and JPA). Also, all the junctions are cross-type structures. The first Al evaporation comes from the top side and the second from the left side in all devices.

The JTWPAs consist of 450 unit cells and the JJ size varies between 1 and 2 μm, each JPA chips consists of 1 JPA coupled to the transmission line and the resonators coupled to a transmission line chip consists out of 31 same-size resonators inductively coupled to a CPW. Note that the middle resonator (so the sixteenth, see Fig3.28) has a capacitance that is halved compared to the other resonators. This was done on purpose to extract the Q-factor during the cryogenic measurements.

To conclude this section we show an overview of the full fabrication process flow in Fig. 3.29. In this figure, we see that after fabrication the measuring part applies which is discussed in the following section.

Figure 3.28: Here we see seven resonators. The middle one is designed to have a different resonance frequency. The Al covers only the half of the dielectric area thereby creating a capacitor with a halved capacitance compared to the other ones.

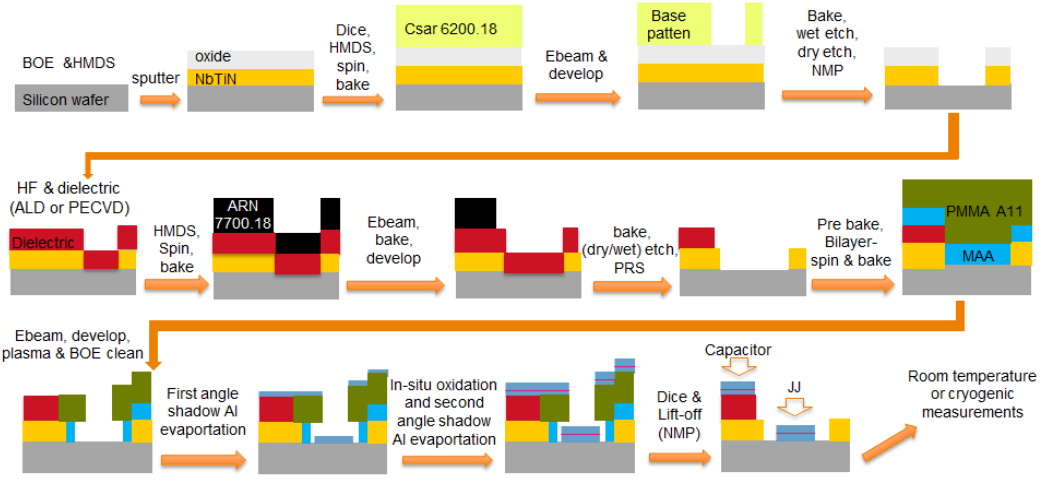

Figure 3.29: Schematic to illustrate the fabrication process of capacitors and JJs. The first row corresponds with the first lithography step. Second lithography step corresponds with the second row except for the last process which is the first process of the third lithography step.

3.3. Measurements

In this section, the setups for both cryogenic and room temperature measurements are described.

3.3.1. Cryostat

The microwave devices fabricated in this thesis requires cryogenic temperatures to become superconducting. The NbTiN 100 nm film has a typical critical temperature of 14-15 K and aluminum 1.25 K. To achieve these low temperatures we mostly used an Oxford Instruments Triton dilution refrigerator. This cryostat uses a refrigeration technique known as helium-3-helium-4 dilution to reach the ≈20mK base temperature. Another cryostat called the Oxford Instruments HelioxVT was used for the first couple of measurements. This cryostat was used to find the resonances of the first couple of resonator samples fabricated in the cleanroom. It uses a helium-3 evaporation refrigeration technique which reaches a base temperature of ≈270mK. However, only the setup of the Triton will be briefly explained as this system was used to characterize the JPA and JTWPA. The interested reader is advised to read [32] which is a textbook that describes the details about these refrigeration techniques.

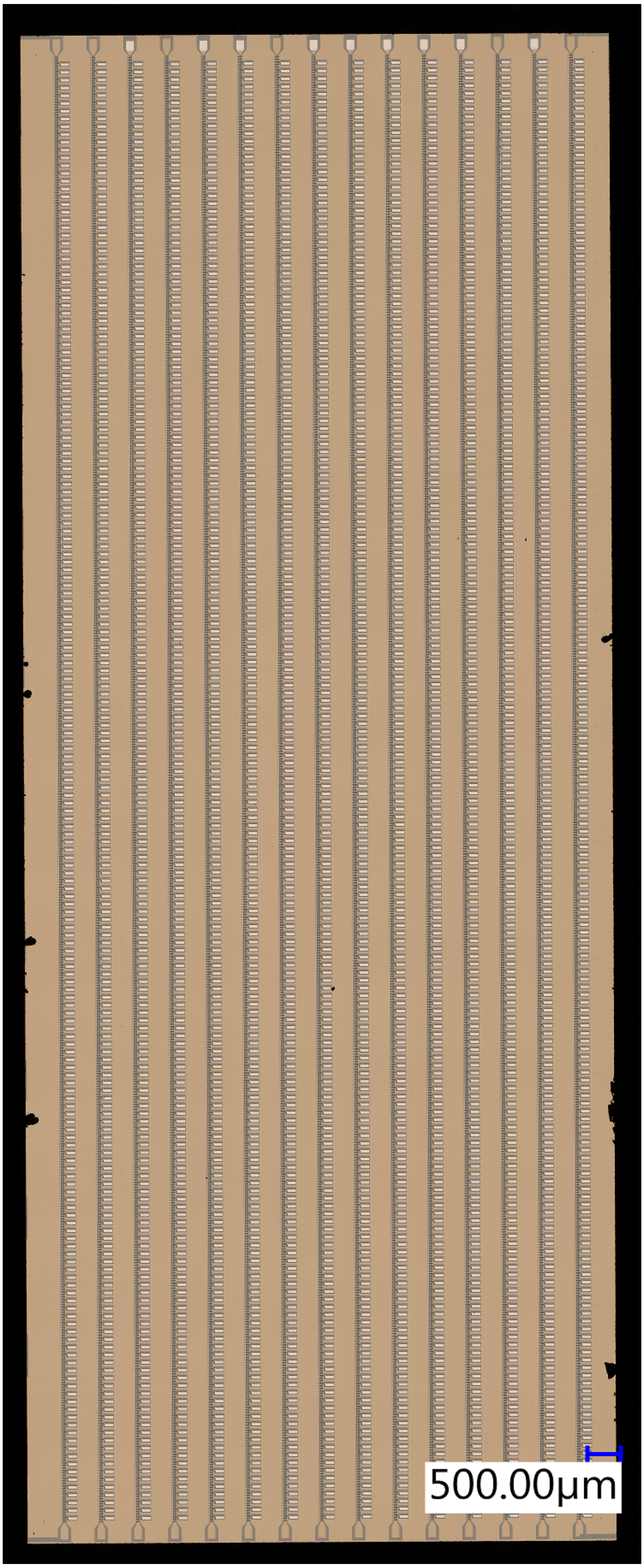

Figure 3.30: The 15 fabricated JTWPAs on one 1 × 3 cm chip.

Experimental setup

In general, dilution refrigerators consist of several plates, each with its own stable temperature such that the temperature declines in several steps from room temperature to the required base temperature. For the cryogenic measurements we basically have two signals (the probe and pump signal) traveling together in one input line Fig. 2.2. These two signals are coupled together with a directional coupler at room temperature (300 K). From the directional coupler the signals continue as one input to the cryostat. The wiring of the cryostat is illustrated in Fig. 3.31.

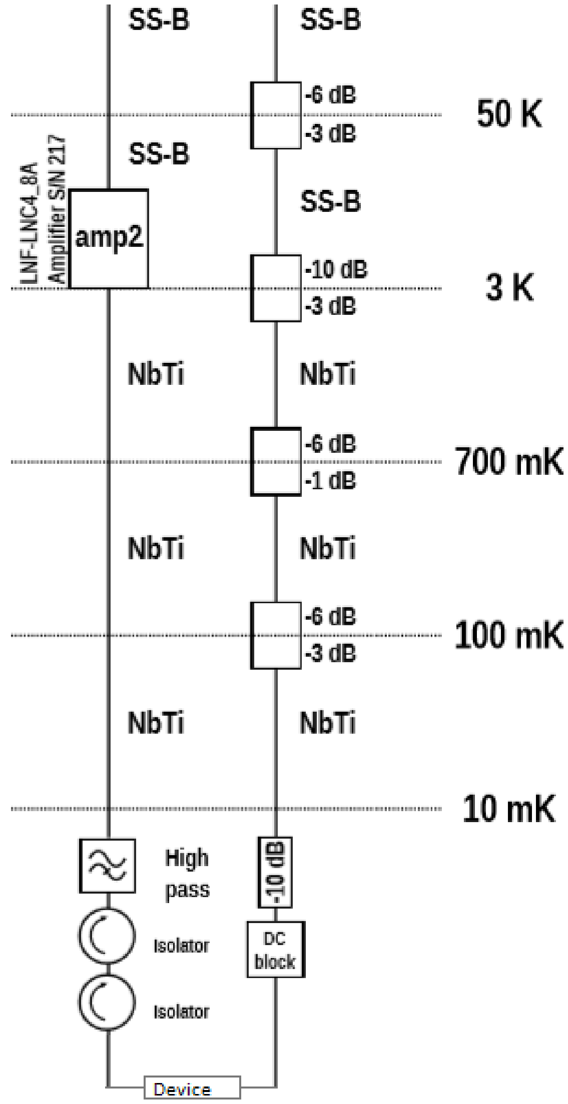

Figure 3.31: Wiring of the Oxford Instruments Triton dilution refrigerator. SS-B and NbTi refer to the materials of the wires. There is a total of -48 dB attenuation inside the refrigerator for the input signal (right line). The amplifier depicted with "amp2" is a HEMT which introduces 42 dB amplification. The Triton cryostat attenuates the signal with 6 dB.

At every stage before the sample the input signal gets attenuated. In the mixing chamber (10 ml) there is a DC block before the signals reach the sample. The DC block is a coaxial component that prevents direct current (DC) to reach the sample while offering minimum interference to RF signals. In addition to this we also have two bias tees. Once the signals passes the sample there are two isolators and a high pass filter. The isolators prevent reflections from propagating back in to the sample because they are directional they also shield the sample from thermal noise coming from the HEMT. Before the signal leaves the cryostat it gets amplified by the HEMT placed in the 3 K stage which amplifies the signal with 42 dB gain over the 4-8 GHz bandwidth. When the signal is out of the cryostat it is amplified again using a room temperature amplifier before it goes to the read out system. The read out equipment is either a VNA or a Spectrum Analyser (SA).

Sample preparation

There are some critical steps to properly connect the samples to the measurement setup of the cryostat. The first step is to wire-bond the sample on a PCB. Wire bonds connect the transmission line of the sample to the transmission line of the PCB. The PCB transmission line is connected to the central pin of a microwave port (SMA-connector) which allows the use of coax cables while the ground is connected to the PCB. The PCB is placed in a copper holder with a lid on. The holder shields the sample from any background radiation. This holder is then mounted inside a puck. For the JTWPA measurements, aluminum foil is used as additional protection against magnetic fields before the puck is connected to the final shield.

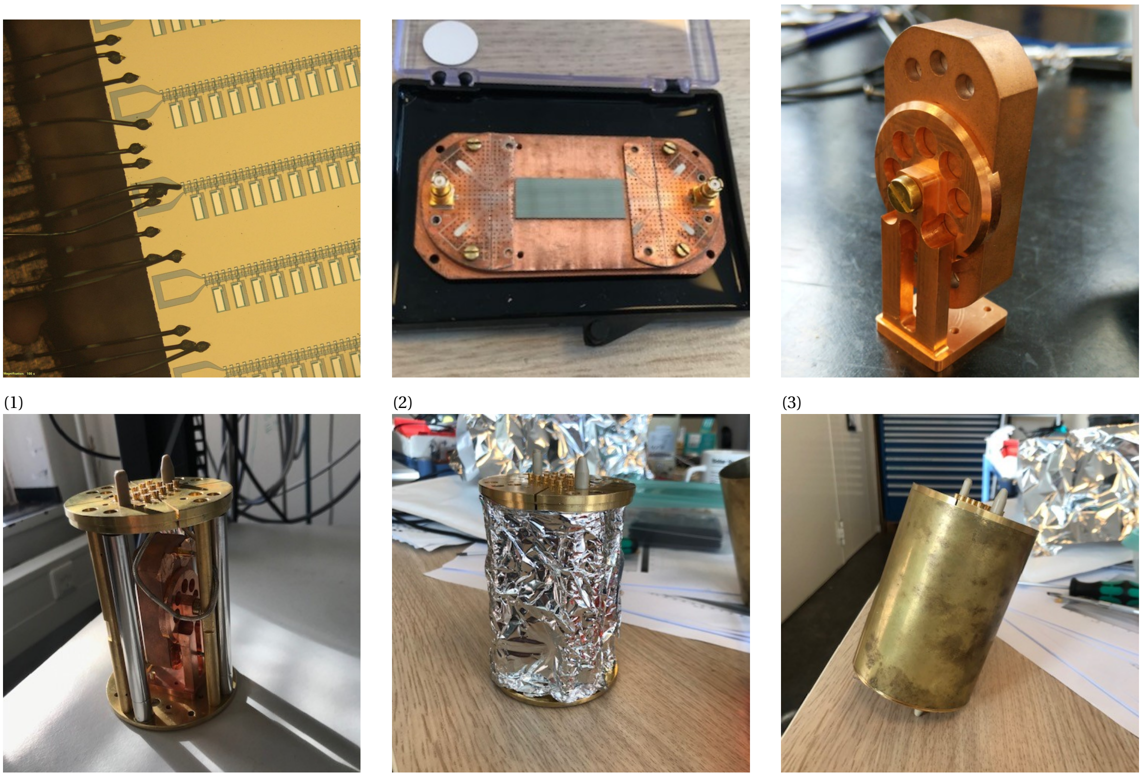

(1) (2) (3)

(4) (5) (6)

Figure 3.32: (1)Sample with fabricated JTWPAs, each has different JJ sizes. The wire bonds are thin aluminum wires which are placed with a ultrasonic needle.(2) PCB used for the JTWPA measurements, the SMA-connectors are the gold connectors on the left and right of the PCB.(3) The copper holder and (4) how it is placed inside the puck.(5) Normal aluminum foil wrapped around the puck. Only for the JTWPA cooldown.(6) The total packaging used to mount the sample in the cryostat.

For the resonators and JPA measurements, we used a different PCB (shown in Fig. 3.33) which is more compatible with the size of the chip. The procedure is largely the same as the JTWPA. We did not use an extra layer of aluminum foil for the JPA as we want to use an external magnetic field.

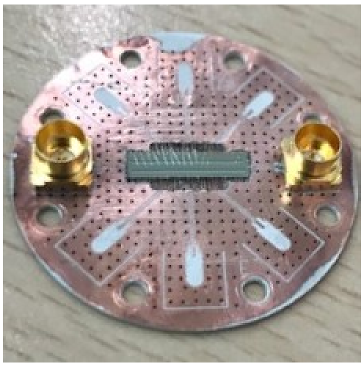

Figure 3.33: PCB used for the resonators and JPA measurements.

3.3.2. Probe station

The probe station is mainly used in this thesis for measuring the resistance of the Josephson junction at room-temperature and for checking whether there is electronic contact between the two probes. Using manipulators we can position precisely two thin tungsten needles. Each needle will go on a probe area connected to the junction or just a surface on the sample to check for electrical contact. When the probes have made contact with the NbTiN probe area, a DC current will flow from one probe to the other, in case of a closed circuit. A normal multimeter would put too much current through the junction which will damage it. This is why the probe needles were connected to a custom-built junction measurement box. With this setup we can determine the resistance over the junction while delivering minimal voltage. These room-temperature measurements are used to target the critical current as the measured resistance is related to the critical current with Eq. 2.21. However, the probe station is not automated so the number of measurement points is limited. The probe station can also be used for quick failure analysis of the devices. The junctions can for instance be open or shorted. Instead of loading the device in an SEM and checking every single JJ, we could also use the probe station which is faster and more flexible to use. Checking the device is important as the time for dilutional fridge measurements is very limited. Another test performed with this setup is to check which orientation of the test capacitor structures (discussed in 3.1.3) is shorted. These structures are probed to check if the Al covered the different transitions (from Si to NbTiN/aSi:H or from NbTiN to aSi:h), see Fig. 3.34. One probe was placed on the Al and the other on the NbTiN, we want this to be an open circuit otherwise, there is no capacitor. In another test, we placed on probe needle on the big Al square and the other on the capacitors Al top plate to check if it is an open or a short circuit. If the circuit is shorted we have good step coverage.

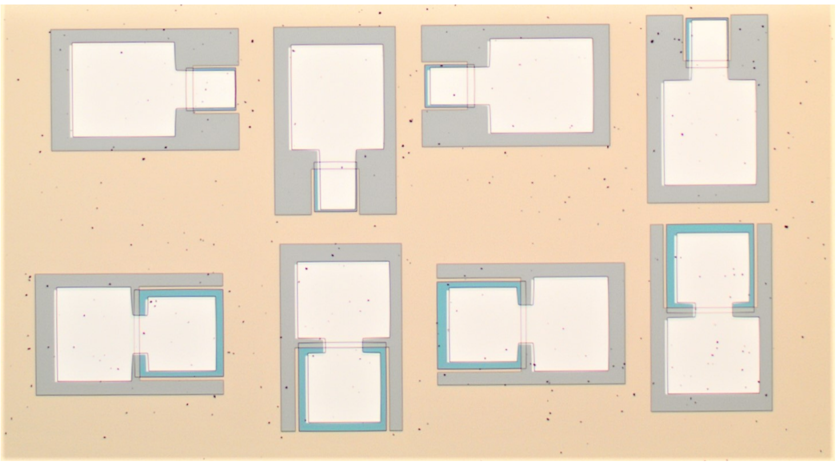

Figure 3.34: The fabricated test capacitors to check which orientation has the best step coverage. The capacitor is formed with NbTiN as a ground plate (gold), aSi:H as dielectric (blue) and Al as a top plate (white). We have two rows, the capacitors in the top are smaller than the capacitors in the bottom. The black dots on the surface come from unknown contamination. This was an intermediate fabrication cycle, this contamination was not found in the last cycle.

4

Results

In this chapter the results from the cryogenic and room temperature measurements are presented.

4.1. Targeting the Josephson critical current

As mentioned before, the Josephson junction is the most critical nano-scale structure in this thesis. The JJs are important in our devices as they provide the non-linearity needed for parametric amplification. However, it is still challenging to reliably produce large numbers of well-targeted and functional Josephson junctions. This section will describe the JJ analysis performed during the thesis.

4.1.1. Room temperature characterization

The room temperature measurements were performed using a probe station, subsection 3.3.2. With the use of two probe needles in contact with the probe areas, a small DC current is sent through the junction which can ultimately be traced back to the normal state resistance (R_n). Measuring an intentionally large sweep of JJ widths, ranging from 100 nm to 6 μm, we were able to observe the limits of this technique, opens and shorts, see Fig4.1.

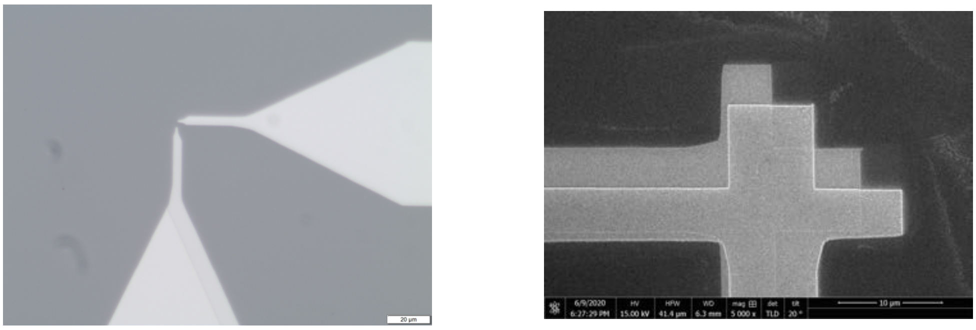

Figure 4.1: 100 nm open JJ (left) and 5 μm shorted junction (right). The two Al lines in the open junction do not overlap, therefore creating a open circuit when measuring. In the shorted JJ we have one JJ line contacting both probe areas letting current pass without tunneling.

First we did a large sweep of 0.1 μm to 4 μm with steps of 100 nm on both sides of the JJ with the resist stack sizes shown in Fig. 3.23. We observed that the JJs with width sizes under 0.4 μm were open and sizes above 2.4 μm shorted. The lowest critical current estimated by this method 0.30 μA (for 0.4 μm JJ) and the highest 6.0 μA (for 2.4 μm JJ). The critical current is calculated with Eq.2.21. The JJ is also expected to be shorted above 2.4 μm due to the geometry of the bilayer, see Fig. 4.2.

It is hard to get a well targeted JJ from only room temperature measurements. The normal state resistance depends on more than just the current through the JJ. Light from the microscope or from the background (measurement room) can change the measured resistance. Another thing to take into account is the placement of the probe needles. The electrical path depends on how far apart the probe needles are placed. Keeping the placement of the probe needles fixed is almost impossible as the NbTiN probe area is sometimes hard to probe whereby the needles are then scraped against the side of the NbTiN. This is done to create a better

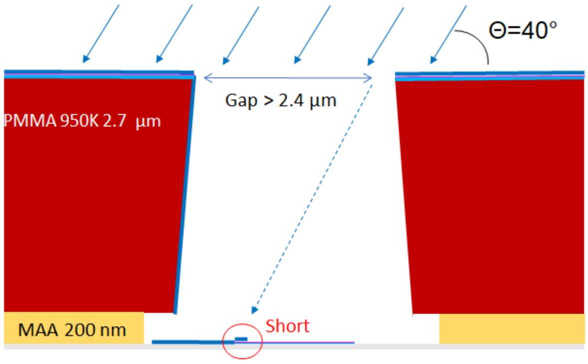

Figure 4.2: Sketch to illustrate shorted JJs.

contact for the probe needles. A dust plug could also stick to one of the probe needles. This is then visible with the microscope and the effect of the plug is also measured because the JJ resistance gets a sudden increase. To remove this plug, the needle must be cleaned with IPA for which we are required to remove the needle from its current position and to wipe it with a IPA napkin. Another reason for JJs being difficult to target is due to the aging phenomena [23]. The oxygen in the barrier slowly migrates in normal room conditions. This causes a slow increase in the normal state resistance with time. This change in resistance could double its value within days. One could anneal the JJs after fabrication to stabilize its value [33]. However, this process has not been applied to the thesis. The long JJ arrays could however tell us something about the relative standard deviation (RSD≡ $\sigma_{I_c}/\langle I_c\rangle$) the JJs can have which is a useful parameter when simulating device such as the JTWPAs. We measured three arrays with different overlap areas. JJs with overlap areas corresponding with 1×1 μm, 1.5×1.5 μm and 2×2 μm were made. This was chosen as the 4.6 μA target value was estimated to lie in that range. Fig. 4.3 shows a histogram of the measured JJ arrays with different JJ sizes. In each array, 100 JJs were measured across an area of 625 mm^2. The 1 μm JJs resulted in 11% RSD, 1.5 μm in 6.8% and 2 μm in 3.6% in critical current. The maximum deviation in the critical current we found is 1.17 μA for the 1×1 μm JJs, 0.52 μA for 1.5×1.5 μm and 0.20 μA for 2×2 μm. Another thing to note is that of the 300 JJs, no open or shorted JJs where measured, resulting in a yield of 100%.

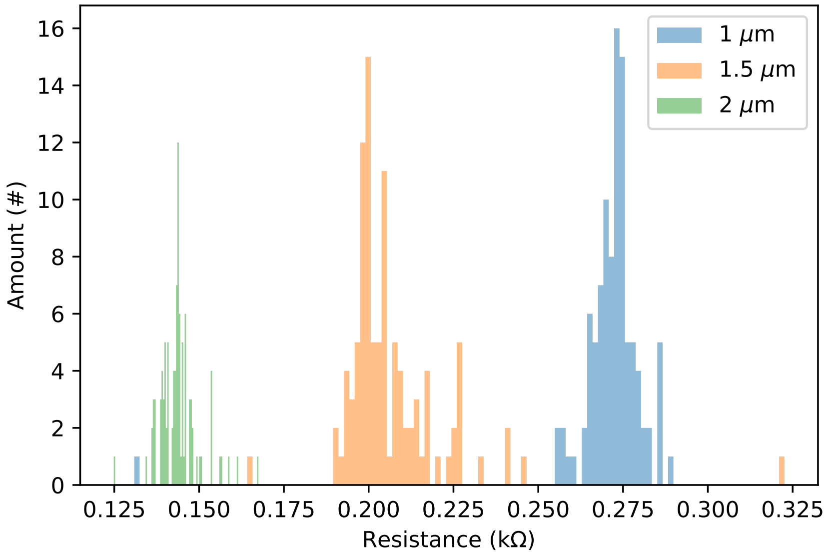

Figure 4.3: The histogram shows 100 RT resistance measurements for each JJ array.

4.2. Lumped element LC resonators coupled to a CPW

The LC resonators sample was measured in the HelioxVT dilution fridge at a base temperature of ≈270mK. The results will be discussed in this section. The simplified schematic is shown in Fig. 4.4[2].

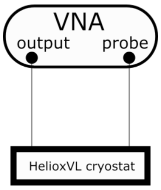

Figure 4.4: The measurement setup for the HelioxVL measurements. The VNA sends a probe signal through the cryostat containing our resonators chip inside and then the signal is read out in the VNA.

In the HelioxVL there is 56 attenuation at the input and 40 dB amplification on the output. Both input and output, are connected to the VNA. The VNA is manufactured by Keysight Technologies and measures in general, both power and phase properties.

4.2.1. Targeting of the resonance frequency

As mentioned before a chip was made with 30 identical resonators plus one "isolated" resonator. The isolated resonator was made with halved capacitance (halved the area A in Eq.3.2) so that we would measure an isolated resonance at a higher frequency as shown in the insert of Fig. 4.5. This isolated resonance is used to fit and extract the internal Q-factor which can be used to provide some measure of the loss tangent (loss of the dielectric inside the capacitor).

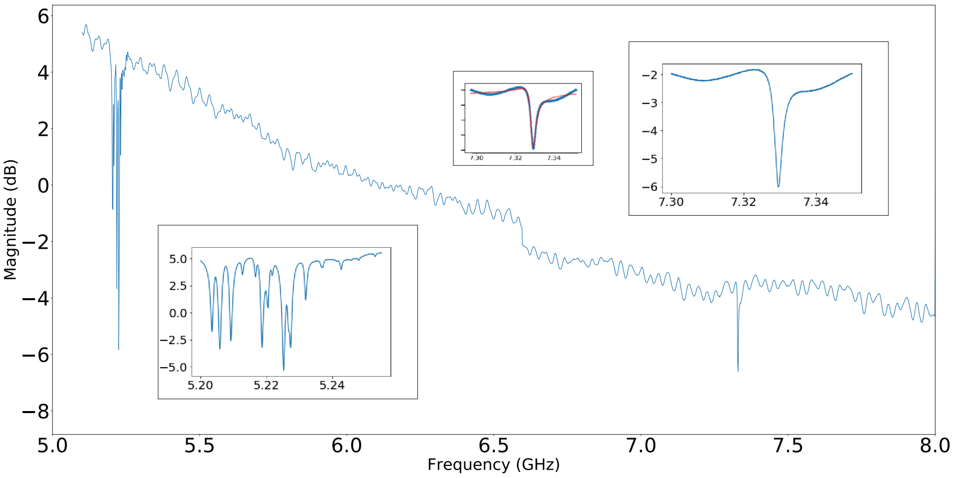

Figure 4.5: Here we see one broad frequency sweep from 5 GHz to 8.5 GHz. The 30 ideally identical resonators have resonant frequencies varying from 5.2 GHz to 5.3 GHz, as the left zoom-in insert shows in the figure. The isolated resonance frequency of the resonator with a halved capacitor can be found in the right insert in the figure. In the middle insert we fit the isolated resonance measurement (red line).

The resonators are 1 GHz off compared to the SONNET simulation shown in Fig. 3.6. This could be due to a miss assumption of the dielectric constant or a incorrect estimation of the kinetic inductance of the NbTiN film. Nevertheless, we fabricated resonators within the 4-8 GHz band which is key for the devices such as the JPA and JTWPA. From the left insert we learn what the spread in fabrication is for the resonators. The spread is almost 50 MHz which corresponds with either <2% deviation in capacitance or inductance. Even though 30 identically resonators were coupled to the CPW, only 19 distinct features can be identified. Some resonant frequencies may overlap with each other causing some resonances to be indistinguishable. The isolated resonance frequency is also measured but at a higher frequency (7.3 GHz) which is as expected since the capacitance is halved. Using a fitting procedure we found $Q_{int} = 3537$ which corresponds with a loss tangent of $\delta = 0.000222$. The transmission is fitted using the Diameter Correction Method (DCM) presented in [21] (Eq. 16 in this paper). However, making a reliable fit is difficult due to crosstalk causing Fano resonances [21] so this is only a indication.

---

[2] The VNA model is ENA Network Analyzer E5080A 9kHz-9GHz, Keysight

4.3. Performance JPA

In addition to measuring the resonators, we also measured a JPA in the HelioxVT, using the same setup as shown in Fig. 4.4. The HelioxVT does not only differ in base temperature from the Triton. The HelioxVT setup does not have an external magnetic field, unlike the Triton. This means that the magnetic field sweep measurements could not be taken. We, therefore, did a VNA measurement to check if the device was worth measuring in the Triton. The measured resonance frequency is shown in Fig. 4.6.

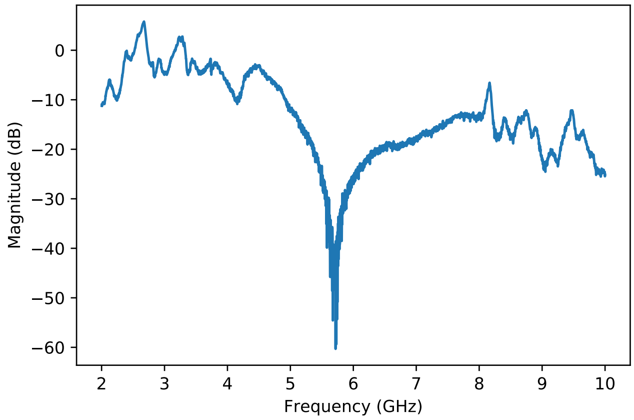

Figure 4.6: JPA resonance frequency measured at ≈270 mK in the HelioxVL cryostat.

Note that the resonance frequency is higher than the resonances we measured for the resonators. This is unexpected as the areas and so the values for the inductance and capacitance are he same in both designs. We expected to find a lower resonance frequency for the JPA as we added a SQUID in series with the inductance, see circuit diagram of the JPA in Fig. 3.8. Hereby adding the Josephson inductance to the inductance of the resonator and lowering its resonance frequency. After finding the resonance frequency we decided to further characterize the JPA in the Triton.

4.3.1. Flux sweeping the SQUID

After two weeks, the same JPA device measured in the HelioxVL was placed inside the Triton cryogenic system and cooled to a base temperature of 14 mK. Fig. 4.7 is a schematic overview of the experimental setup[3][4].

The first measurement performed is a magnetic field sweep of ± 0.25 mT, while measuring S_{21} power in dB over a frequency range of 3.2 to 4.6 GHz, see Fig. 4.8.

The measured resonance frequency with a changing external magnetic field never exceeded 4.4 GHz. Which is odd as we measured a resonance frequency of 5.8 GHz during the HelioxVT measurement. A possible explanation for this permanent shift in resonance is the aging of the Josephson junctions in the SQUID [23]. There were two weeks between the HelioxVT and Triton measurements with the JPA sample stored outside the cleanroom in atmospheric pressure. Aging of the JJs should increase their normal state resistance [23], this decreases the critical current (according to Eq.2.21) which increases the Josephson SQUID inductance (according to Eq.2.28) therefore decreasing the resonance frequency (according to Eq.2.29). Another mystery is the jumps in resonances when sweeping the external magnetic field. These jumps could indicate that the SQUID suffers from hysteresis effects. However, this seems unlikely since we minimized the screening parameter β_l during the design to prevent this effect. Another explanation for the flux jumps is the flux focusing effect caused by quantum vortices. The aluminum used for the JJs inside the SQUID is a type 1 superconductor which is not affected by the magnetic field. However, the NbTiN is a type 2 superconductor which allows the formation of magnetic field vortices with an applied external magnetic field. In Fig. 4.9 the measured JPA is shown with the SQUID loop indicated with a blue circle. The JJs forming the SQUID are made out of Al which are connected to the ground plane. This geometry results in a SQUID loop partially made out of NbTiN, which is the ground plane, causing these flux jumps. The flux jumps make it difficult to extract the periodicity using a fit. However, the measurement seems to have an estimated periodicity of 45 μT which is

---

[3] SMB 100A Signal Generator 100kHz-12.75GHz, Rohde & Schwar

[4] Room temperature amplifier model: LNA-30-04000800-07-10P

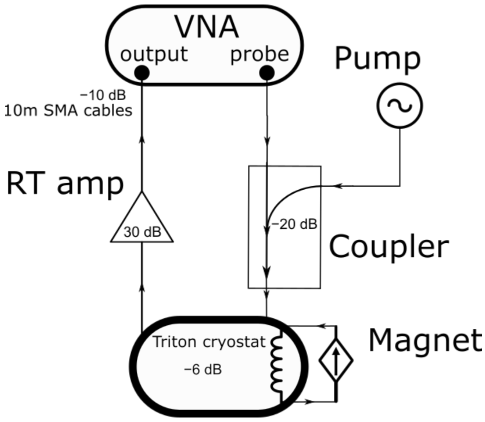

Figure 4.7: Experimental setup diagram for the Triton VNA measurements. The magnet introduces an external flux bias used for flux sweeping the SQUID in the JPA device. The magnet is connected to a Keysight power source, which provides a constant current over a superconducting coil. The RF power source labeled as pump is a signal generator used during gain measurements. The probe and pump signals are coupled together with a Krytar directional coupler which introduces -20 dB attenuation to the pump signal only. The signal then goes through the dilution fridge (wiring for this is shown in Fig. 3.31), to a room temperature amplifier (RT amp) which adds 30 dB (over the 4-8 GHz bandwidth) to the signal before it goes to the readout system. The coax cables outside the cryostat introduce an additional attenuation of -10 dB (cable length ≈ 11 m).

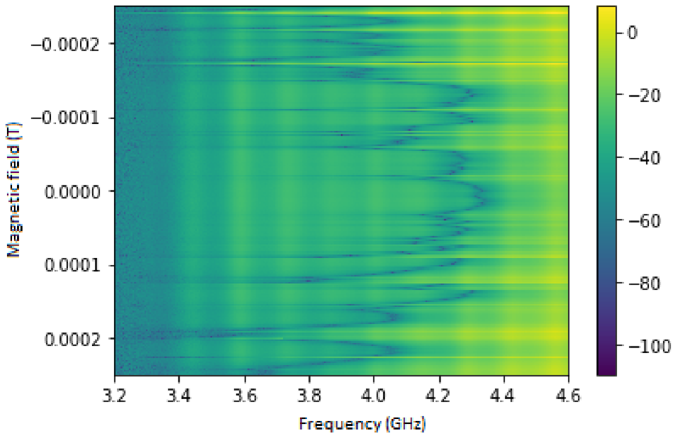

Figure 4.8: Magnetic field scan. The color scale bar shows the power in dB, the y axis shows the field in tesla (T) and the x axis shows the frequency range over which we measured.

not similar to what we would expect. We expected periodicity of 90μT. This together with the corresponding $25\mu m^2$ (SQUID loop area) will give $1.088\ \Phi_0$ (with Φ_0=magnetic flux quanta using 3.6). The flux penetrating the SQUID loop might be doubled due to the flux focusing effect.

4.3.2. Probe power scan

The magnetic field is now kept to a constant value while we check what happens over a broad range at higher probe power. Important to note that the mentioned power (in dBm) is the power at room temperature.

A power scan at a specific field shows odd high power behavior. At applied probe strengths above 5 dBm, the resonance frequency disappears and the signal is 20 dB higher. This has led us to believe that the coupling capacitor is microshorted, indicated with the red circle in Fig. 4.9. This is probably a design error, the Al should have been evaporated only on the top of the couple capacitor but as can also be seen in the optical image, there is a small step coverage to the NbTiN ground plane. The hypothesis for the 30 dB loss in transmission is that the JPA is strongly coupled to the CPW causing reflection. The microshort can be seen as an inductor for small probe signals. However when the JPA is exposed to higher probe powers the current through this inductor exceeds its critical current and so it becomes non-superconducting, therefore resistive. When this is the case, a large part of the input signal skips the JPA and will only pass through the superconducting CPW. The higher probe signal measurement is also comparable with a through measurement shown

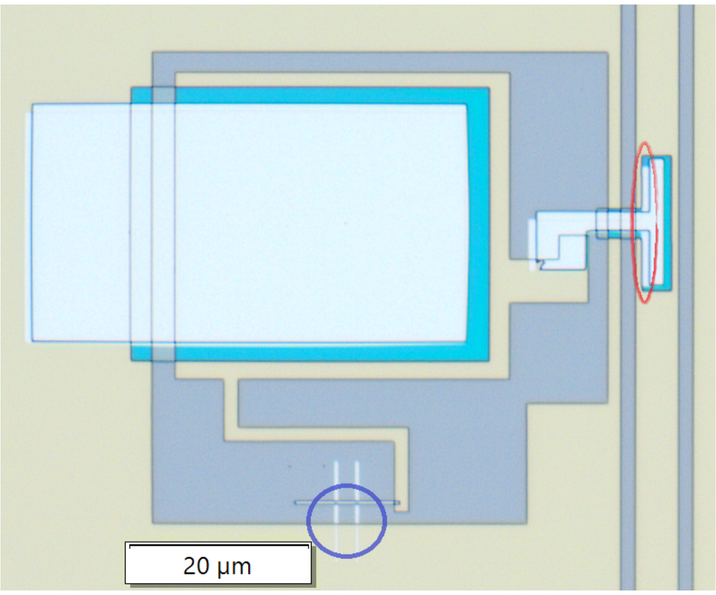

Figure 4.9: The JPA device. The blue circle indicates the SQUID loop consisting out of Al and NbTiN. The red circle indicates where we expect to have a micro short in the couple capacitor. This capacitor couples the JPA to the CPW.

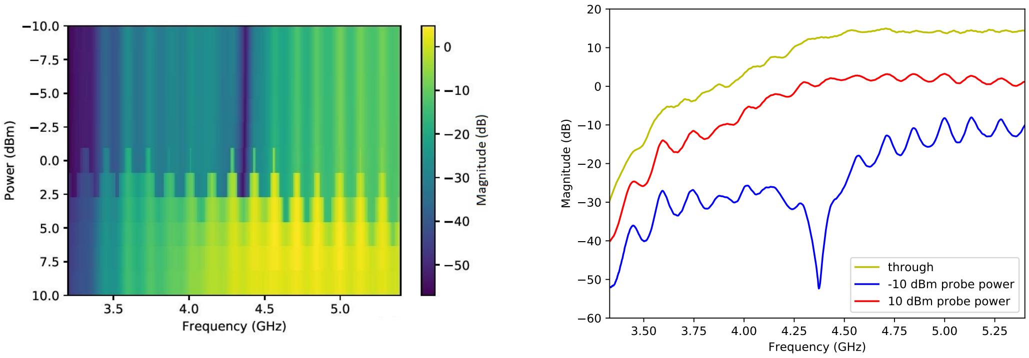

Figure 4.10: The probe power is swept from -10 dBm to 10 dBm for a frequency range of 3.25 to 5.5 GHz (left). The color scale indicates the power difference measured by the VNA in dB. Three graphs, low power, high power and for comparison a through measurement (right). For the through measurement, the PCB containing the JPA was unloaded and a through cable was put inside the puck. For the rest of the transmission the same setup and cables are used so it should be a good reference measurement.

in Fig. 4.10. The through measurement is done to understand how the system as a whole behaves taken into account the cryostat plus RT components like VNA, amplifiers, etc. The through measurement indicates that the JPA with a high probe power acts like a through.

JPA measurements involving a pump are shown in the appendix B. These measurements are not consistent with the gain-bandwidth product. This is a fundamental constrain to the JPA, discussed in theory chapter 2.5.

4.4. Performance JTWPA

The fabricated JTWPA which we will characterize in this section has 150 unit cells which corresponds to 450 JJs in series, Fig. 3.10 shows the circuit diagram of one unit cell. For the JTWPA we started again measuring with a VNA setup Fig. 4.7. The difference in setup compared to the JPA is that we did not use the external magnetic field as the JTWPA does not contain any SQUIDs. As additional shielding for external magnetic fields we used aluminum foil, see Fig. 3.32(5). In order to get a reference to the background for all measurements, the transmission through the cable through was compared with the transmission through the JTWPA with no pump, see Fig. 4.11.

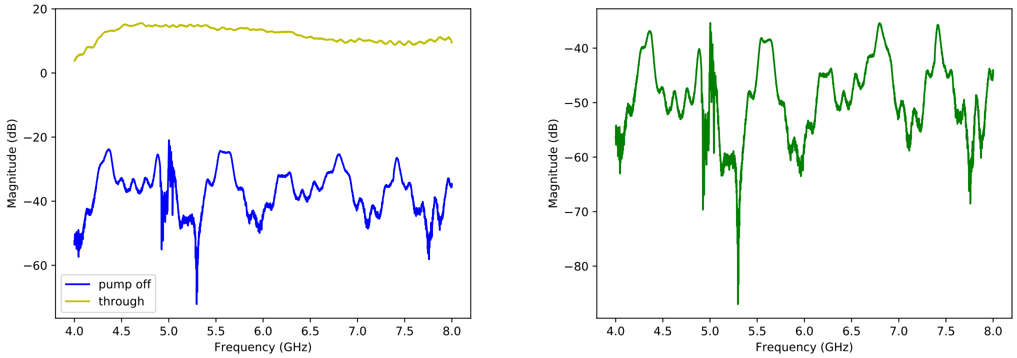

Figure 4.11: The through cable and the through JTWPA measurement linecuts (left). The transmission loss of the JTWPA, calculated as the through JTWPA without pump minus the through cable measurement (right).

We observe dips around 5.2 GHz which is consistent with the resonator measurement we did in the HelioxVL. The resonators do not contain any aluminum like the JPA so we did not expect any shifts in resonances caused by aging. Another notable thing is that we found the transmission line to be very phase mismatched indicated by the ripples. Looking at the difference of the through and transmission measurement (green graph) we see that the transmission is on average -50 dB and the ripples are around 10 dB. -50 dB is a great decrease in transmission power and could indicate that we have loss somewhere in the JTWPA.

4.4.1. Simulation JTWPA transmission

The JTWPA was inspected with an optical microscope after the cryogenic measurements to find possible defects that could explain the high transmission loss. A remaining piece of NbTiN that contacts the central part of the transmission line with the ground plane has been found, see Fig. 4.12.

Using a ABCD scattering matrix model we can simulate the expected device performance in a through measurement. The model sees the JTWPA as a linear system so the Josephson junctions are replaced with linear inductors in the unit cells, see Fig. 3.10 for the schematic of the unit cell. Filling in the relevant parameters (explained in the appendix A) we simulated the transmission for three cases:

- With a capacitor added in series in the middle of the JTWPA (red curve). Simulating the case of an open JJ in the transmission line.
- With a shunt inductor to ground in the middle of the JTWPA (blue curve).
- With a shunt resistor to ground in the middle of the JTWPA (green curve).

The first thing to notice in all curves is the dip in transmission at 5.2 GHz, which could represents the dispersive feature. We introduced a capacitor, inductor or resistor to find some quantitative values for possible defects that can cause some loss in transmission. We estimate the value of these elements that would correspond with the -50 dB transmission loss we measured in Fig. 4.11. A 2 nF capacitor in the red curve represents effectively an open JJ. The transmission improve (so reflection decreases) with increasing frequency as the electrical impedance decreases, consistent with Eq. 2.17. The blue curve models the JTWPA with a 5 pH shunt inductor to ground which could be a representation of the defect shown in Fig. 4.12. However narrow connections can cause a huge kinetic inductance in a realistic superconducting circuit. A small current could be enough to exceed the critical current of the NbTiN thereby changing the defect into a resistor to

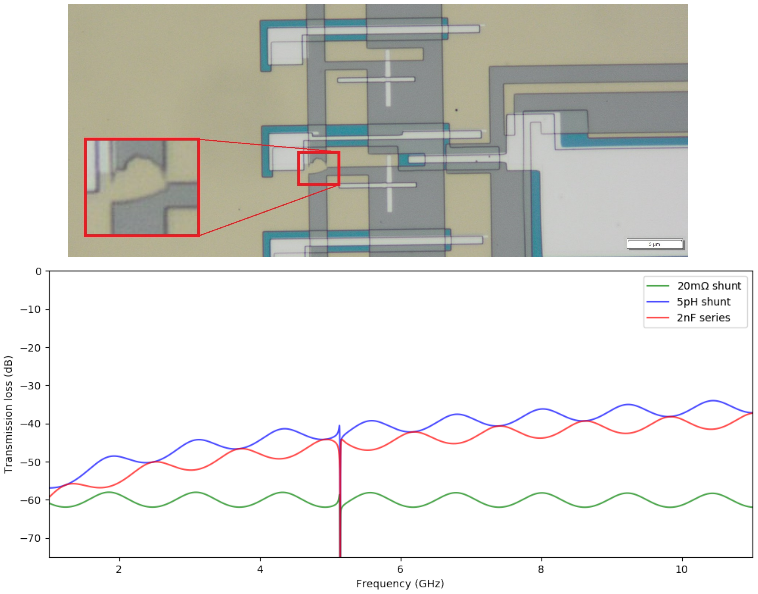

Figure 4.12: The NbTiN defect taken taken with a optical microscope (top). Three simulated transmission graphs through a JTWPA without a pump (bottom).

ground. Including a 20 mΩ resistor in the model, we found transmission of -50 dB. The electrical impedance of a resistor is not frequency depended so we do not expect to see a dependence in frequency. One could use a Focused Ion Beam (FIB) to locally mill this NbTiN defect. The FIB uses a focused beam of ions to remove materials, in our cause NbTiN. Remeasuring the same JTWPA device in cryogenic temperatures after a FIB process would be a good way to see if our transmission loss hypothesis is correct. This did unfortunately not fit within the planning of the thesis. Moreover, we had fabricated a total of 15 JTWPA devices on the same substrate. We have wirebonded an adjacent device with slightly different JJ size and no visible defects in the base layer upon optical inspection. But again, due to time limits, this measurement is still pending.

4.4.2. Probe power scan

We also did a measurement where we swept the probe power to check for shifting features like for the JPA.

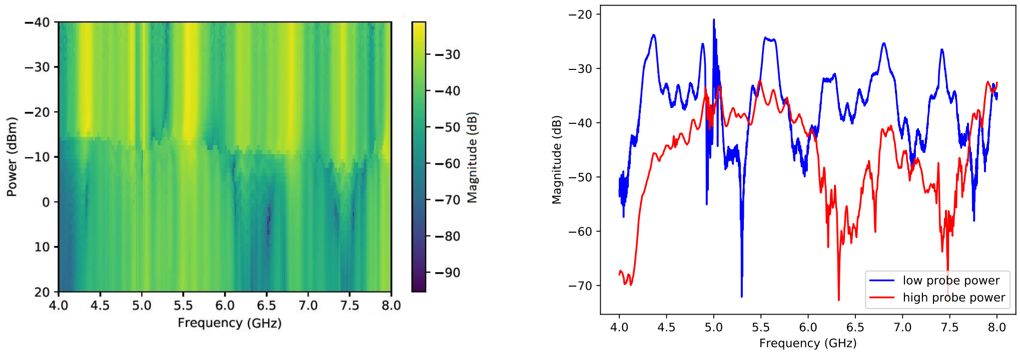

Figure 4.13: The probe power is swept from high power 20 dBm to low power -40 dBm (left). The average magnitude for low probe power signals is -35 dB and the average magnitude for high probe power signals is -45 dB (right).

The low power probe line cut is similar to the transmission line cut we used in Fig. 4.11. Even though the resonance frequency disappeared like in the JPA measurement (Fig. 4.10), we found that applying a high probe power to the JTWPA lowers the averages transmission with 10 dB, see the right plot of Fig. 4.13. The readout starts to decrease in transmission if the probe power is higher then –10 dBm which is labeled as the high probe power regime. Notice also some shift in resonance frequency (around 5.2 GHz) in the region of

-20 dBm and -10 dBm. It could be the non-linearity of the kinetic inductance that is causing the resonance frequency of the RPM resonator to shift at higher powers.

4.4.3. JTWPA two tone measurement

We used a signal generator to pump the JTWPA. To characterize the gain profile we first swept the pump frequency with different pump powers. Fig. 4.14 shows one sweep with 10 dBm pump power. Second, we selected a pump frequency and swept the pump power. We found high gain at 4.7 dBm pump power. The right plot shows the line cut for this pump power and the line cut without pump for comparison.

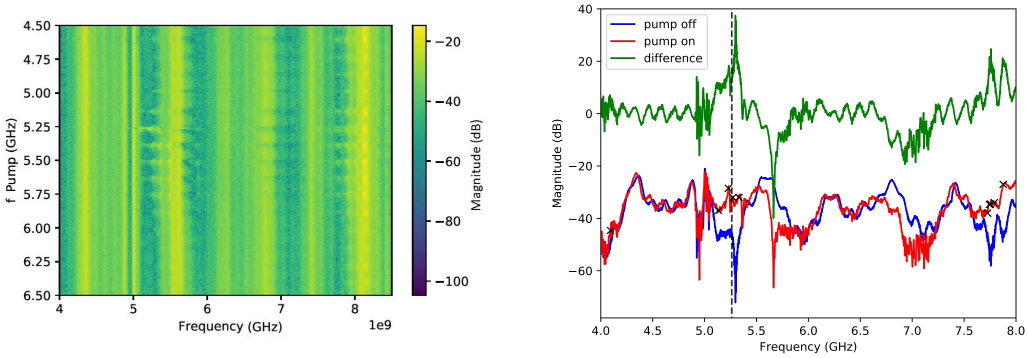

Figure 4.14: First, the pump frequency with a constant pump power is swept and the transmission is measured (left). Two line cuts for a different measurement where the pump frequency was constant and the pump power was swept (right). The blue graph is the transmission without a pump and the red graph is the transmission with a pump power of 4.7 dBm. Ten gain points on this graph are selected (indicated with X), which will be analyzed further. The dashed line indicated the pump frequency 5.262 GHz. The green graph is the difference between the two transmission lines.

The sweep measurement suggests that we can pump the JTWPA over a wide frequency range. First, we swep the pump frequency while keeping the pump power constant and then we performed another measurement in which we fixed the pump frequency at 5.262 GHz and swept the pump power. In the right plot of Fig. 4.14 we see gain areas in between 5.05 and 5.35 GHz and 7.6 and 8 GHz. Ten points are selected, five are in the lower frequency band and five in the higher frequency band. These points are analyzed further with a spectrum analyzer.

4.4.4. indication of Josephson traveling wave parametric amplification

Now we include a SA as depicted in Fig. B.2. We performed sweeps by varying only the probe frequency and applying a fixed power of the probe and pump signals using again two signal generators, shown in Fig. 4.15.

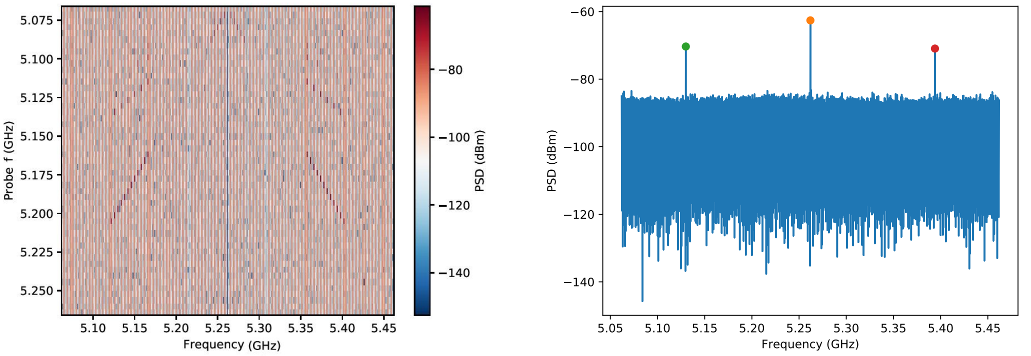

Figure 4.15: Color scaled plot varying the probe frequency in the y axis, the measured frequency range is the x axis and the color indicates the measured power (left). The right diagonal line represents the idler and it symmetrically follows the probe signal which is the left diagonal. Line cut of the SA measurement (right). The appearance of the idler (red dot) at the opposite side of the probe signal (green dot) with respect to the pump (orange dot), shows that we can operate our JTWPA as a four wave mixer. Note again the wavy noise floor.

We put our probe frequency at 5.229 GHz, which is a point in the gain band shown in Fig. 4.14, and investigate with the SA. By turning the pump off and on we can extract the saturation power and the SNR improvement (ΔSNR) at this specific frequency. We will go through the analysis of measurements with the probe frequency at 5.229 GHz and pump frequency at 5.262 GHz. Fig. 4.16 shows the saturation powers for both 1 dB and 3 dB compression points.

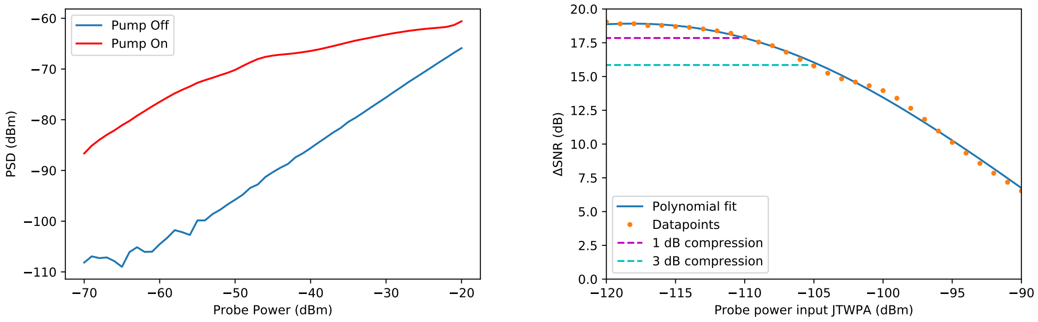

Figure 4.16: Two compression curves where we measure the probe power at 5.229 GHz with and without a pump (left). The ΔSNR as a function of the probe power at the input of the JTWPA (right).

The 1 dB compression point is -109 dBm and the 3 dB compression is -104 dBm assuming that the probe signal is attenuated by -53 dB (cryo line down = -48 dB and input cable outside fridge = -5 dB). The saturation power at this specific frequency is lower than the JTWPA presented in this paper [25] which had a saturation power of -98 dB.

Next step is to calculate the ΔSNR which is a measure by how well the SNR improved using the JTWPA. The same data is used as for the saturation measurement but now we look at a narrow frequency range of 100 kHz around the probe frequency to have a measure of the noise floor in order to find the SNR, see Fig. 4.17. The power of the probe signal is defined as the max value of the plot and the noise floor is defined as the average value of the rest of the data points. The SNR is defined as the probe power minus the noise floor, in dB.

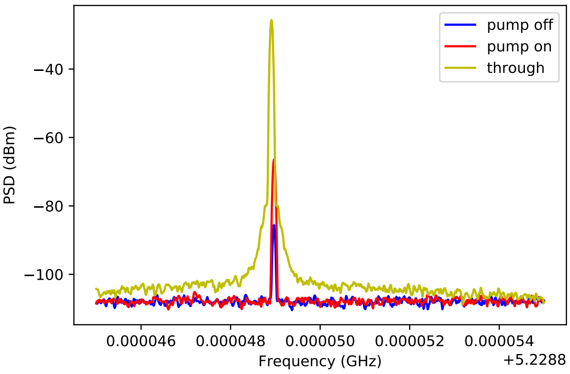

Figure 4.17: Three transmission measurements shown to extract the SNR. The y-axis is the PSD of the probe at 5.229 GHz. Blue graph is the transmission with pump off, red is with pump on and yellow is a cable through SA measurement at 5.262 GHz. The corresponding SNR values are 22.4 dB, 41.3 dB and 77.7 dB respectively.

We measured an increase of 18.9 dB when comparing the SNR of JTWPA with and without the pump. This is ΔSNR for the probe signal at 5.229 GHz with a pump at 5.26 GHz. The ΔSNR relative to the cable through measurement is 55.3 dB, which is high compared to ΔSNR as we expect to have in average 50 dB loss in the transmission of the JTWPA. In table 4.1 the measured ΔSNR, 1 and 3 dB compression points are shown for ten different probe frequencies.

Table 4.1: Results of SA analysis for multiple probe frequencies. The measurements where performed with a pump frequency of 5.262 GHz and power of 4.7 dBm.

Probe frequency (GHz)	**Gain** (dB)	**ΔSNR** (dB)	**1 dB compression** (dBm)	**3 dB compression** (dBm)
4.094	2.4	3.2	-91	-82
5.134	11.6	16.1	-95	-90
5.229	16.4	18.9	-110	-105
5.273	18.3	15.4	-84	-79
5.332	16.8	17.1	-115	-106
7.726	10.9	9.7	-93	-87
7.744	20.1	20.2	-93	-87
7.753	17.6	18	-93	-87
7.791	13.9	17.2	-87	-83
7.877	20	12.8	-90	-84

4.4.5. Unexplained features of the JTWPA

The pump frequency is changed to check if the JTWPA can be driven on a wide frequency range which the VNA measurement already indicated, see Fig. 4.14. We kept the probe frequency the same (5.229 GHz) but measured two different pump frequencies, 5.262 GHz and 5.51 GHz. The probe power is measured while the pump power is swept for both pump frequencies.

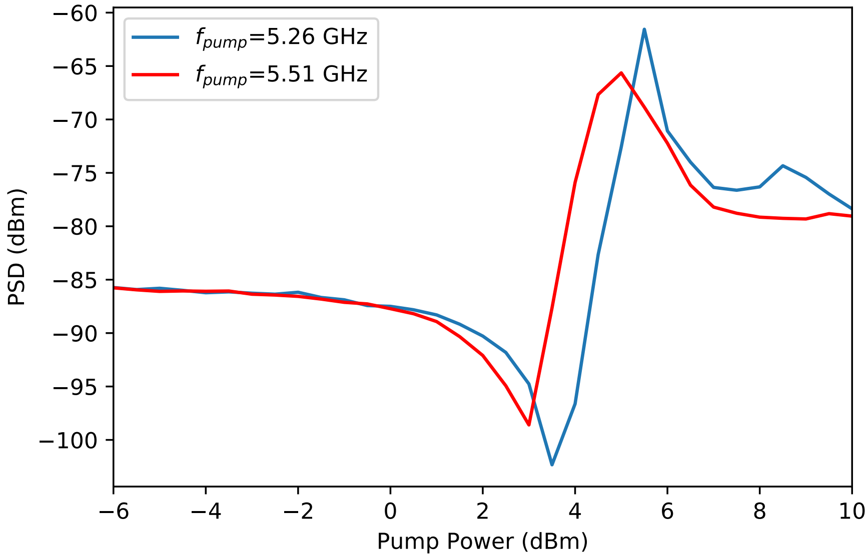

Figure 4.18: SA measurements of probe power scans as a function of pump power. The pump frequency is 5.262 GHz (blue curve) and 5.51 GHz (red curve). The pump is off below 0 dBm.

Fig. 4.18 shows a 20 dB increase in SNR at two different pump frequencies 5.262 GHz and 5.51 GHz. A possible explanation for the ability to drive our JTWPA on multiple pump frequencies is the spread in RPM resonant frequencies according to [30]. The spread in these resonators actually allows us to pump our JTWPA in multiple frequencies. However, the spread also creates a large stopband in the middle of the gain curve. Another interesting feature is that the JTWPA deamplifies before it amplifies when the pump power is increased. An explanation for this is still unknown.

5

Conclusion

The goal of this thesis was to create Josephson parametric amplifiers with a new fabrication method. In this chapter, we will recap the work and discuss the results found in this thesis.

5.1. Fabrication process improvements

In total, we fabricated four types of devices that we could measure and characterize. Josephson junctions, lumped element LC resonators, JPAs and JTWPAs. Several fabrication issues are found and solved in all three lithography steps.

In the first fabrication cycle, we observed "cookie crumbles" on the Si areas of the samples after the NbTiN layer etch. The defects could be from the resist reacting with the plasma or ion bombardment of the SF_6/O_2 dry etch. We decided to partially etch the NbTiN base layer with a SF_6/O_2 dry etch and finish with a wet etch consisting of ammonia, peroxide and water to avoid the "cookie crumbles". This resulted in smoother Si surfaces (see Fig. 3.13) after the base layer patterning.

The second lithography step was dedicated to fabricating the dielectrics for the capacitors, see subsection 3.2.2. We tried multiple etch processes and the etch with CHF_3/O_2 gasses resulted in the smoothest surface, see Fig. 3.17. We also invested some time in fabricating the devices with ALD AlOx instead of PECVD aSi:H. However, due to errors showing up during the wet etch of this dielectric made the devices impractical within the time frame of this thesis, see Fig. 3.20.

In the third and last lithography step, the JJs and the top plates of the capacitors were defined. The aluminum JJs are deposited using a double-angle evaporation method for which is based on a bilayer of resist. However, after developing this bilayer, we found cracks in the resist next to the exposed areas. Using a cold developer instead of a room-temperature developer we got rid of the cracks, see Fig. 3.21.

5.2. Josephson Junctions

The Al-AlOx-Al Josephson junctions fabricated in this thesis are known as "Manhattan Style" junctions or cross junctions. The bridge-less fabrication method used to fabricate the JJs uses shadows from a pre-patterned bilayer of resist. First, a large sweep of different JJ overlap areas was fabricated to find what the limit is of the designed JJs. The smallest working JJs had a overlap area of 0.4×0.4 μm ($I_c = 0.30$ μA) and the largest JJs had a area of 2.4×2.4 μm ($I_c = 6.0$ μA). The goal was to fabricate JJs with $I_c \approx 4.6$ μA which successfully is in between the largest and smallest JJ. To determine the stability of the JJs we designed and fabricated three long arrays with overlap areas of 1×1 μm, 1.5×1.5 μm and 2×2 μm. We measured 100 JJs from each array to calculate the relative standard deviation (RSD$\equiv \sigma_{I_c}/\langle I_c\rangle$), see Fig. 4.3 which shows three histograms of the measured JJs. The 1 μm JJs resulted in 11% RSD, 1.5 μm in 6.8%, 2 μm in 3.6% in critical current and the yield of the measured JJs is 100%. We found the smallest RSD for the biggest JJs, as expected.

5.2.1. Discussion JJs

It is important to note that the room temperature measurements are not accurate enough to tell us what the critical current exactly is. The normal state resistance can be influenced by different factors like the light in the measurement room, different electrical paths between the two probe needles, dust plugs on the probe needles and aging of the JJs. To get a higher resolution of the critical current one could do a switching current measurement [43]. This is a cryogenic measurement which requires DC lines with sufficient DC filtering inside a cryostat with a base temperature of $T \approx 280$ mK. Once the critical current of the JJ is well-targeted one could again fabricate long arrays of the same size JJs to find their stability. However, instead of a manual probe station, one should use an automated one to get a better measure of the RSD and yield of the JJs. An automated probe station can easily measure a full wafer of JJs which will give a better measure of the stability of the JJS.

5.3. Lumped element LC resonators

The LC resonators are important to characterize as both the JPA and JTWPA use these. The development of these resonators started by simulating two models with SONNET. First a CPW with a NbTiN ground plane and second an LC resonator coupled to a CPW with aSi:H as a dielectric. The goal of these simulations was to gain qualitative insight into what the parameters and dimensions roughly should be. The closest match to a 50 Ω transmission line is when the CPW has two gaps of 4 μm separated by a middle part with a width of 12 μm, see Fig. 3.3 and 3.4. For the resonator, we found a resonance frequency at 6.23 GHz, see Fig. 3.6 and 3.5 for the design. Using the dimensions of the simulation we successfully fabricated 31 resonators coupled to a CPW with resonances in the 4-8 GHz sweet spot. Although the resonator model was simple and the parameters used were not exactly like reality, the qualitative behavior of the simulated resonator close to the measurements. We measured resonant frequencies varying from 5.2 to 5.25 GHz in the HelioxVL cryostat, see Fig. 4.5. This spread corresponds with <2% deviation in capacitance or inductance. Using a fitting procedure known as the Diameter Correction Method we found Q_{int}=3537 which corresponds with a loss tangent of $\delta =$ 0.000222.

5.3.1. Discussion resonators

Making a reliable fit is difficult due to crosstalk causing Fano resonances. This makes it hard to characterize the dielectric loss tangent precisely. One could fabricate another chip with varying resonators coupled to a CPW instead of identical ones. This can be done by either varying the capacitance (changing capacitor area) or the inductance (changing length of the meander) of the resonator. With a chain of resonators varying in steps of for instance 5%, one can compare the designed deviation in L or C with the measured one. Another more important aspect of this experiment is the higher possibility that one could find resonance frequencies who are not suffering from crosstalk. These resonances could easily be fitted to have a more accurate measure of the Q factor and calibration of the loss tangent.

5.4. Josephson Parametric Amplifier

The JPA sample measured in both the HelioxVL and Triton cryostats consisted out of a lumped element JPA capacitively coupled to a CPW. The JPA device was first measured in the HelioxVL where we found a resonance frequency at 5.8 GHz, see Fig. 4.6. Two weeks later we measured the same sample in the Triton and found resonance frequencies < 4.4 GHz while doing a magnetic flux sweep with an external magnetic inside the cryostat, see Fig. 4.8. This change in resonance has led us to suspect that the JJs forming the SQUID loop of the JPA suffered from aging. The periodicity of the changing resonance frequency during the magnetic flux sweep measurement is twice the expected value. This is assumed to be caused by the NbTiN ground layer due to the flux focusing effect. After the magnetic field sweep measurements, we kept the flux constant and studied the limits in terms of pump and probe power. At applied probe power above 5 dBm (generator output) the resonance frequency disappears and the transmission increases by 20 dB over a band of 2.5 GHz, see Fig. 4.10. This is not the behavior we would expect from a JPA and we suspect that there is a microshort in the couple capacitor. What we suspect to happen is that for low powers the JPA resonates but with a 30 dB loss in transmission as a great amount of the signal is going to ground through the JPA. This makes the JPA directly coupled to the CPW instead of capacitavly coupled. When higher powers are applied the microshort effectively changes from an inductor to a resistor. This causes the signal to pass through the CPW without going to the JPA. Which could explain the measurement was comparable with the through measurement. This is all speculation, we do not know for sure if there is a microshortage at the couple capacitor.

Another set of measurements involving a pump are shown in the appendix B. In the two tone measurement where we swept the pump frequency we observed that it is possible to pump the device over a wide range of frequencies (over a 2 GHz band) and observe "gain" which is odd behavior for a JPA, see Fig. B.1. It should not be possible to drive the JPA outside the cavity bandwidth and observe gain. The SA measurements (see Fig. B.4 for set up) showed some four wave mixing, see Fig. B.3. However, if the JPA was causing the four wave mixing, it would not make sense, to see it outside the cavity bandwidth set by the gain-bandwidth product fundamental to the JPA. The non linearity needed for the four wave mixing could originate from any non linear component in between the signal generator and spectrum analyser. Possible explanation could be that the four wave mixing is caused by the non linearity of a saturated HEMT amplifier.

5.4.1. Discussion JPA

The long-term stability of the JPA device can be improved by implementing a reliable housing/protection technology as well as annealing the JJs forming the SQUID. Annealing of the JJs should prevent the JJs from aging making them better to target. To avoid the flux focusing effect during the flux sweeping measurements one should probably adjust the design of the JPA in a way to create a SQUID loop only out of aluminum. One should also change the couple capacitor design to prevent the microshortage. This could be fixed by making the area of dielectric covered by the aluminum counter electrode a bit narrower, leaving an increased safety margin and increase tolerance to lithographic misalignments. The two parts of the JPA device which need to change for a better performance are indicated with circles in Fig. 4.9.

5.5. Josephson Traveling Wave Parametric Amplifier

Another outcome of this project is the JTWPA. We tried to recreate the JTWPA discussed in this paper [25] but with a different fabrication method. The JTWPA fabricated and measured in this thesis consisted out of 150 unit cells (so 150 RPMs, 450 JJs and shunt capacitors). The used JJs overlap area was 1.5×1.5 μm and the JTWPA had a total length of 2 cm. The JTWPA was measured inside the Oxford Instruments Triton cryostat but without any use of a external magnetic field. We measured a 50 dB loss in transmission and 10 dB ripples compared to the through measurement, see Fig. 4.11. The ripples indicate that the transmission is poorly phase matched this is probably caused by badly targeted Josephson inductance of the JJs. We checked the JTWPA with a optical microscope and discovered that the transmission line was contacting the ground via a piece of NbTiN which could explain the 50 dB transmission loss, see Fig. 4.12. We simulated the transmission through the JTWPA without a pump using a ABDC scattering matrix model according to the circuit diagram shown in Fig. 3.10 [6] with the parameters shown in table A.1. We found that a loss of 50 dB in transmission which could corresponds with a 20 nΩ resistor to ground or a 5 pH inductor to ground or a 2 nF capacitor in the middle of the transmission line. We think that the resistor to ground matches the defect the best as we do not see any increase in transmission with higher frequencies. Another reason is the high kinetic inductance in the NbTiN. A small current could be enough to exceed the critical current of the defect thereby changing it to a resistive state. From the probe power scan measurement we found that the transmission decreases if the probe power is higher then -10 dBm (generator output), see Fig. 4.13. Right before the transmission decreases we measure a shift in resonance frequency around 5.2 GHz which is where we expect our dispersive feature to be. It could be the non-linearity of the kinetic inductance that is causing the resonance frequency of the RPM resonator to shift at higher powers. The two tone measurements that we did showed that the JTWPA could be driven with a pump over a wide frequency band, see Fig. 4.14. The theory in [30] suggests that the JTWPA can be current pumped at multiple frequencies if the spread of the resonators is large. However the spread in resonators measured in the HelioxVL is 50 MHz which is smaller than the 2 GHz frequency sweep of the pump frequency. So, a good explanation for why we can pump the JTWPA over this hide frequency range remains unknown. In another two tone measurement we swept the pump power while we kept its frequency constant at 5.262 GHz. By subtracting a line cut from this measurement and comparing it to a line cut from a JTWPA measurement without a pump we found two areas where we have higher transmission i.e. gain. We selected in total ten points, five in the lower frequency band of 5.05 to 5.35 GHz and five in the higher frequency band of 7.6 and 8 GHz, to analyze further with a SA. The reason why the transmission is amplified in these bands and deamplified in other band remains unknown. Moving on to the SA measurements we started by applying a fixed power of the probe and pump signals and kept the pump frequency constant while we swept the probe, see Fig. 4.15. The appearance of the idler at the opposite side of the probe with respect to the pump frequency indicated that we can operate the JTWPA as a four wave mixer. However it is important to note that the non

---

[6] The simulated model is a linear JTWPA circuit so the non linear Josephson junctions are replaced with linear inductors.

linearity could come from a other component in the transmission like a saturated HEMT amplifier causing the wave mixing. From ten selected point we calculated the 1 ΔSNR, 1 dB and 3 dB compression points, see table 4.1. From these measurements we can conclude that the transmission profile is frequency depended when changing the probe power. By looking at the difference of the 1 dB and 3 dB compression points for the ten frequency points we find that (especially for the lower five frequency points) the transmission changes unevenly. Also the ΔSNR differs at different frequencies, since the JTWPA amplifies differently at different frequencies. The highest ΔSNR reached is 20.2 dB at 7.744 GHz.

5.5.1. Discussion JTWPA

The transmission through the JTWPA compared to the transmission through the cable is always lower. We suspect that this is due to the NbTiN shortage to ground. One could us a FIB to locally etch away this defect. By removing the NbTiN one could check and prove if the loss in transmission was caused by this defect. Another possibility is to wirebond another JTWPA as we fabricated 15 JTWPAs on the same chip. The same measurements can be performed however one should take into account that every JTWPA on the chip has a different JJ overlap area. The different JTWPAs can be measured to find the transmission with the smallest ripples i.e. the transmission with the best characteristic line impedance. To have a better understanding of the optimal performance of the JTWPA one should preform more measurements to compare different gain profile with each other. This did not fit within the scope of this thesis.

6

Outlook

This chapter will provide an general outlook for future research on the various devices developed in this thesis. There are also a few suggestions for future work to be found in the discussion subsections of the previous chapter.

Improving the uniformity of the NbTiN film. The sheet kinetic inductance $L_{k,s}$ typically varies 10% across the 4-inch wafer. This can be problematic for large structures like the JTWPAs. The variation can be reduced by depositing the NbTiN with ALD instead of sputtering [40]. Another option is to chemical mechanical polish the film after deposition. However, the Kavli nanolab does not posses the machinery for this.

Fabricate JPA devices with no Josephson junction. These would provide a good calibration of the Josephson inductance of the JJs.

Fabricate resonators with interdigitated finger capacitors. The resonators would provide an good calibration of the kinetic inductance of the NbTiN film and of the dielectric constant of the dielectric used in the resonators with the parallel plate capacitors.

Include a local flux line on the JPA chips. This would give the flexibility of using the JPA for flux pumped amplification (three wave mixing mode).

Fabricate devices with different dielectrics and deposition processes. One should aim to find a uniform process to reduce the spread in resonators. By comparing different dielectrics, one can also find a dielectric that has the least loss, which will improve the JTWPA performance. Incorporation of ALD dielectric (like AlOx) and its loss tangent extraction will be definitely interesting in the project continuation.

Consider a JTWPA design with finger capacitors, in cause the dielectric loss is the limiting factor of the device. This alternative would reduce the fabrication of the device to two lithography steps. However the finger capacitors use a lot of area which reduces the design to fewer unit cells.

Measure reflection. One could preform a reflection measurement by adding a circulator in front of the JTWPA. Measuring the reflection will allow one to distinguish the internal loss of the JTWPA from the reflection loss. This is important for measurements involving a transmon chip in front of the JTWPA.

Use a integrated through in combination with a cryogenic switch. How we measured the cable through in this work was by unloading the device under testing and then loading a cable. By using a on chip CPW in combination with a cryogenic switch we could choose between measuring the JTWPA and the through. This would provide a better background correction.

A

Simulation JTWPA transmission parameters

The model consist out 150 unit cells. The JJs were simulated as linear inductors with 71.54 nH calculated with Eq.2.25 for 4.6 μA. The model also included the PCB, short wirebonds connecting the PCB to a intermediate PCB and lastly long wirebonds connecting the intermediate PCB to the JTWPA as shown in Fig. 3.32 (1) and (2). However we did not include these parameters in the plots shown in Fig. 4.12 as we did not see major effects.

Table A.1: Model parameters.

Quantity	**Symbool**	**Value**
Josephson Inductor	L_{J0}	71.54 nH
Shunt Capacitor	C_s	45 fF
Thrid shunt capacitor	C_{s3}	25 fF
Couple capacitor	C_c	20 fF
Resonator capacitor	C_r	5.3 pF
Resonator inductor	L_r	180 pH
Loss tangent	δ	0.0003
Long wirebond inductance	L_{w1}	950 pH
Short wirebond inductance	L_{w2}	600 pH
Impedance CPW chip	$Z_{0,chip}$	51 Ω
Impedance CPW PCB	$Z_{0,PCB}$	49 Ω
Capacitance open JJ error	C_{error}	2 fF
Shunt inductor error	L_{error}	5 pH
Shunt resistor error	R_{error}	20 mΩ

B

JPA measurements

This chapter includes some cryogenic measurements for the JPA involving a pump.

B.1. JPA two tone measurement

After the probe power sweep measurements, we turned the signal generator on which will current pump the JPA. During these measurements, we kept the magnetic field to a constant. The pump is attached to the -20 dB line of the directional coupler, as shown in Fig. 4.7. Broad bandwidth measurement sweeping pump frequency, showed repeated intervals of increased transmission, see Fig. B.1.

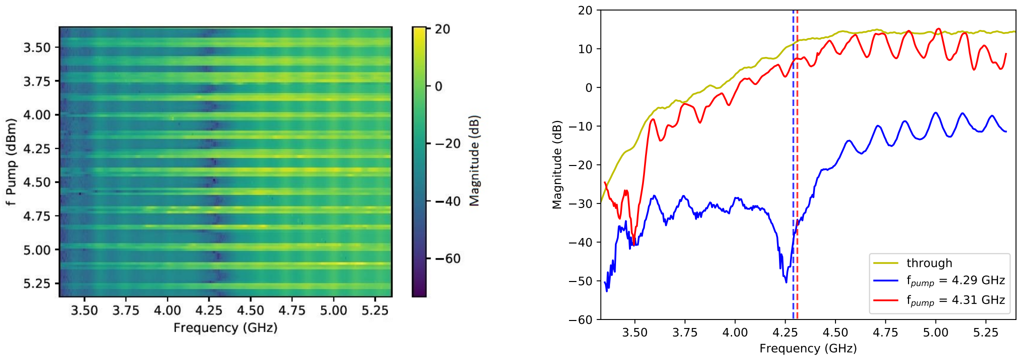

Figure B.1: The pump frequency (f_{pump}) is swept while the probe frequency is kept to a constant value (f_{probe} = 5.2 GHz) (left). We compared two line cuts (f_{pump} = 4.29 GHz and f_{pump} = 4.31 GHz) to a through measurement line cut (right). The dotted lines indicate at which frequency the pump sits.

This measurement is performed with a fixed magnetic field and signal (probe and pump) power. The measurement indicates that the JPA could be driven in multiply pump frequencies which is unusual for JPAs. JPAs typically have a bandwidth of 100-500 MHz and can not amplify outside this bandwidth. This is the limiting factor for all JPAs known as the gain-bandwidth constraint discussed in theory chapter 2.5. Pumping in some frequency bands we observe the same dB attenuation as the low probe power measurement (shown in Fig. 4.10) but when pumping on the right spots we see an increase in transmission of 30 dB, which makes the transmission look like the through measurement.

B.2. Indication of non-linearity

A spectrum analyzer (SA) is used to see if there is any four wave mixing in the JPA device. Two source generators[5] are used, one as pump and another as probe source, see Fig. B.2. A spectrum analyzer measures the Power Spectral Density (PSD) in dBm of an input signal for a set frequency range.

---

[5] SMB 100A Signal Generator 100kHz-12.75GHz, Rohde & Schwar

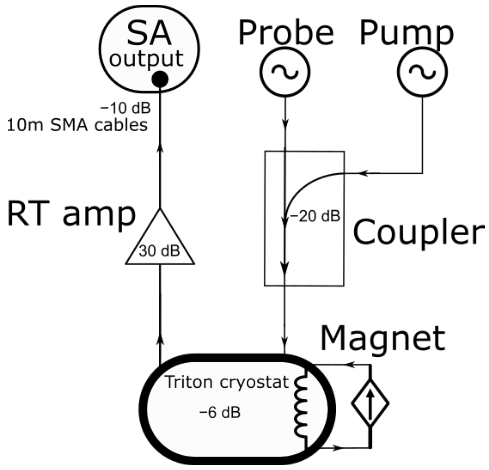

Figure B.2: Experimental setup diagram for the Triton SA measurements. It is similar to the VNA setup (Fig. 4.7) but in this case we used a signal generator for the probe signal and only the SA is connected only to the output.

To observe four wave mixing, the JPA needs to be pumped at resonance. However this is not the case with this measurements. The resonance frequency was around 3.75 GHz but we pumped at 4.8 GHz. The probe signal was swept with the second signal generator and the measured output power is plotted in the color scaled plot shown in Fig. B.3.

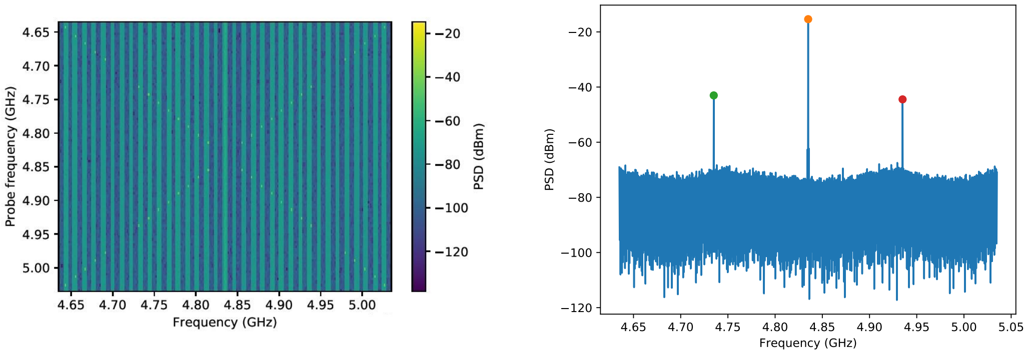

Figure B.3: Color scaled plot showing the varied probe frequency in the y axis, the measured frequency range is the x axis and the color indicates the measured power at the SA (left). The pump frequency is kept constant at 4.835 GHz and the probe frequency is varied from 4.635 to 5.035 GHz in this measurement. The probe power is set to be the same as the VNA measurements, so - 40 dBm output. The linecut at the right shows three pieks. The probe at the right (green dot) and the idler at the left (red dot) are centering the higher pump frequency peak (orange dot) in the middle.

The presence of the idler, and the fact that it moves opposite to the probe signal with respect to the pump, shows that there is four wave mixing. This is not consistent with the gain bandwidth product of the JPA. If the JPA was causing the four wave mixing, it would no be possible to see gain outside the cavity bandwidth. A possible explanation for the four wave mixing observed in this measurement is that the mixing is caused by the non-linearity of a saturated HEMT amplifier but we do not know this for sure. Note that the resolution bandwidth of the SA is smaller than the steps in the probe sweep frequency which is not commensurate with each other. Due to this mismatch of the pump and frequency steps, we observe a wavy noise floor. Nevertheless, we continued by trying to find the saturation power. This we did by sweeping the pump power while keeping its frequency constant (f_{pump} = 4.8 GHz) and measuring the probe power at one frequency (f_{probe} = 4.1 GHz). In Fig. B.4 two line cuts are plotted, the probe power is measured with and without a pump.

As expected we see an increase in PSD of about 35 dBm when comparing the measured probe power with and without a pump. This measurement does not indicate any saturation behavior. JPAs typically saturate around -130 dBm. For this system that would correspond to an output power of -87 dBm, taking into account

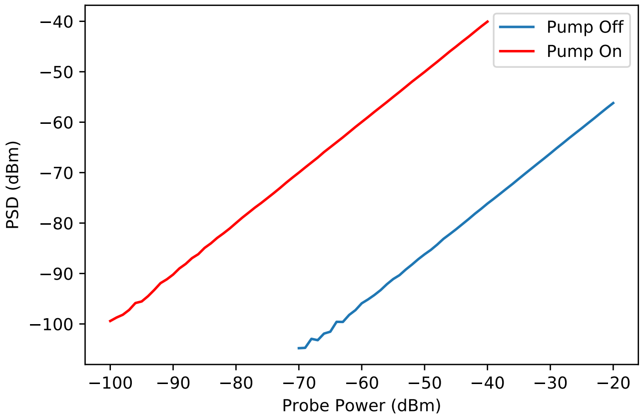

Figure B.4: Two line cuts of the measured power vs the probe power are plotted. X-axis is the probe power generated by the signal generator. Y-axis is the PSD measured by the SA.

the attenuation of the wiring inside the cryostat (Fig. 3.31) and the cables outside the cryostat (Fig. B.2). However the linecut taken from the measurement with the pump on (red line) does not show any indication of saturation behaviour (the red line is super linear). This is yet another indication that the JPA might be shorted to the transmission line.

Bibliography

[1] A compact design for the josephson mixer: The lumped element circuit. *Appl. Phys. Lett. 106*, pages 45–49, 2015.

[2] V. Ambegaokar and A. Baratoff. Tunneling between superconductors. *Erratum Phys. Rev. Lett.*, 11: 486–489, 1963.

[3] Anthony J Annunziata, Daniel F Santavicca, Luigi Frunzio, Gianluigi Catelani, Michael J Rooks, Aviad Frydman, and Daniel E Prober. Tunable superconducting nanoinductors. *Nanotechnology*, 21(44): 445202, Oct 2010. ISSN 1361-6528. doi: 10.1088/0957-4484/21/44/445202. URL `http://dx.doi.org/10.1088/0957-4484/21/44/445202`.

[4] J. Aumentado. Superconducting parametric amplifiers: The state of the art in josephson parametric amplifiers. *Journal of Applied Physics*, 21(8):45–49, 2020.

[5] A. Barone and G. Paternò. Physics and applications of the josephson effect. *New York : Wiley*, 1982.

[6] Manuel Angel Castellanos Beltran. Development of a josephson parametric amplifier for the preparation and detection of non classical states of microwave fields. *PhD thesis*, 2010.

[7] E. W. Bryerton, M. Morgan, and M. W. Pospieszalski. Ultra low noise cryogenic amplifiers for radio astronomy. In *2013 IEEE Radio and Wireless Symposium*, pages 358–360, 2013.

[8] A. A. Clerk, M. H. Devoret, S. M. Girvin, Florian Marquardt, and R. J. Schoelkopf. Introduction to quantum noise, measurement, and amplification. *Reviews of Modern Physics*, 82(2):1155–1208, Apr 2010. ISSN 1539-0756. doi: 10.1103/revmodphys.82.1155. URL `http://dx.doi.org/10.1103/RevModPhys.82.1155`.

[9] A. CULLEN. A travelling-wave parametric amplifier. *Nature*, 181, 1958.

[10] M. Pozar. David. *Microwave engineering*. John Wiley Sons, Inc., 4th edition, 2012. ISBN 978-0-470-63155-3.

[11] C. Eichler. Quantum-limited amplification and entanglement in coupled nonlinear resonators. *Physical Review Letters*, 113, 2014.

[12] M. J. Feldman. Parametric amplification by unbiased josephson junctions. *Journal of Applied Physics*, 1975.

[13] R. P. Feynman. Simulating physics with computers. *International Journal of Theoretical Physics*, 21: 467–488, 1982.

[14] Sami Franssila. Introduction to microfabrication. 2nd edition. *John Wiley Sons, Ltd*, 2010.

[15] J Ganji, A Kosarian, and H. Kaabi. Mathematical evaluation of a-si:h film formation in rf-pecvd systems. *Silicon*, 12:723–734, 2020.

[16] Jiansong Gao. The physics of superconducting microwave resonators. *Caltech*, 2008.

[17] G. Grynberg. Introduction to quantum optics and lasers. *Superconductor Science and Technology*, 2010. ISSN 9780521551120.

[18] R. C. Jaklevic. Quantum interference effects in josephson tunneling. *Phys. Rev. Lett.*, 12:159–160, 1964.

[19] B. Josephson. Possible new effects in superconductive tunnelling. *Physics Letters*, 1:251–253, 1962.

[20] O.W. Kennedy, J. Burnett, J.C. Fenton, N.G.N. Constantino, P.A. Warburton, J.J.L. Morton, and E. Dupont-Ferrier. Tunable Nb superconducting resonator based on a constriction nano-squid fabricated with a Ne focused ion beam. *Phys. Rev. Applied*, 11:014006, Jan 2019. doi: 10.1103/PhysRevApplied.11.014006. URL `https://link.aps.org/doi/10.1103/PhysRevApplied.11.014006`.

[21] M. S. Khalil, M. J. A. Stoutimore, F. C. Wellstood, and K. D. Osborn. An analysis method for asymmetric resonator transmission applied to superconducting devices. *Journal of Applied Physics*, 111(5):054510, Mar 2012. ISSN 1089-7550. doi: 10.1063/1.3692073. URL `http://dx.doi.org/10.1063/1.3692073`.

[22] R. W. Klopfenstein. A transmission line taper of improved design. *in Proceedings of the IRE*, 44:31–35, 1956.

[23] P. J. Koppinen, L. M. Väistö, and I. J. Maasilta. Complete stabilization and improvement of the characteristics of tunnel junctions by thermal annealing. *Applied Physics Letters*, 90(5):053503, Jan 2007. ISSN 1077-3118. doi: 10.1063/1.2437662. URL `http://dx.doi.org/10.1063/1.2437662`.

[24] J M Kreikebaum, K P O'Brien, A Morvan, and I Siddiqi. Improving wafer-scale josephson junction resistance variation in superconducting quantum coherent circuits. *Superconductor Science and Technology*, 33(6):06LT02, May 2020. ISSN 1361-6668. doi: 10.1088/1361-6668/ab8617. URL `http://dx.doi.org/10.1088/1361-6668/ab8617`.

[25] C. Macklin. A near–quantum-limited josephson traveling-wave parametric amplifier. *Science*, 350:307–310, Sept 2015. ISSN 6258.

[26] Benjamin A. Mazin. Microwave kinetic inductance detectors. *Phd thesis, Caltech*, 2004.

[27] Corey Rae Harrington McRae, Haozhi Wang, Jiansong Gao, Michael Vissers, Teresa Brecht, Andrew Dunsworth, David Pappas, and Josh Mutus. Materials loss measurements using superconducting microwave resonators, 2020.

[28] Alessandro Miano and Oleg A. Mukhanov. Symmetric traveling wave parametric amplifier. *IEEE Transactions on Applied Superconductivity*, 29(5):1–6, Aug 2019. ISSN 2378-7074. doi: 10.1109/tasc.2019.2904699. URL `http://dx.doi.org/10.1109/TASC.2019.2904699`.

[29] YV Nazarov and YM Blanter. *Quantum Transport -Introduction to Nanoscience*. Cambridge University Press, United Kingdom, 2009. ISBN 978-0-521-83246-5.

[30] Kevin O'Brien, Chris Macklin, Irfan Siddiqi, and Xiang Zhang. Resonant phase matching of josephson junction traveling wave parametric amplifiers. *Phys. Rev. Lett.*, 113:157001, Oct 2014. doi: 10.1103/PhysRevLett.113.157001. URL `https://link.aps.org/doi/10.1103/PhysRevLett.113.157001`.

[31] H. K. Onnes. The resistance of pure mercury at helium temperatures. *Commun. Phys. Lab. Univ. Leiden*, 1911.

[32] F. Pobell. Matter and methods at low temperatures. pages 1–461, 01 2007. doi: 10.1007/978-3-540-46360-3_1.

[33] I. M. Pop, T. Fournier, T. Crozes, F. Lecocq, I. Matei, B. Pannetier, O. Buisson, and W. Guichard. Fabrication of stable and reproducible submicron tunnel junctions. *Journal of Vacuum Science Technology B, Nanotechnology and Microelectronics: Materials, Processing, Measurement, and Phenomena*, 30(1):010607, Jan 2012. ISSN 2166-2754. doi: 10.1116/1.3673790. URL `http://dx.doi.org/10.1116/1.3673790`.

[34] N. Simons. Rainee. *Coplanar Waveguide Circuits, Components, and Systems*. John Wiley Sons, Inc., 2001. ISBN 978-0-471-16121-9.

[35] I. C. Rodrigues, D. Bothner, and G. A. Steele. Coupling microwave photons to a mechanical resonator using quantum interference. *Nature Communications*, 10(1), Nov 2019. ISSN 2041-1723. doi: 10.1038/s41467-019-12964-2. URL `http://dx.doi.org/10.1038/s41467-019-12964-2`.

[36] Ananda Roy and Michel Devoret. Quantum-limited parametric amplification with josephson circuits in the regime of pump depletion. *Physical Review B*, 98(4), 2018. ISSN 2469-9969. doi: 10.1103/physrevb.98.045405. URL `http://dx.doi.org/10.1103/PhysRevB.98.045405`.

[37] Flavius Schackert, Ananda Roy, Michael Hatridge, Michel H. Devoret, and A. Douglas Stone. Three-wave mixing with three incoming waves: Signal-idler coherent attenuation and gain enhancement in a parametric amplifier. *Physical Review Letters*, 111(7), Aug 2013. ISSN 1079-7114. doi: 10.1103/physrevlett.111.073903. URL `http://dx.doi.org/10.1103/PhysRevLett.111.073903`.

[38] M. Simoen. Parametric interactions with signals and the vacuum. *Chalmers University of Technology*, 2015.

[39] Daniel Huber Slichter. Quantum jumps and measurement backaction in a superconducting qubit. *PhD thesis*, 2011.

[40] David Thoen, Boy Bos, E.A.F Haalebos, T.M. Klapwijk, J.J.A. Baselmans, and A. Endo. Superconducting nbtin thin films with highly uniform properties over a 100 mm diameter wafer. *IEEE Transactions on Applied Superconductivity*, PP, 09 2016. doi: 10.1109/TASC.2016.2631948.

[41] Sergey K. Tolpygo, Vladimir Bolkhovsky, Terence J. Weir, Leonard M. Johnson, Mark A. Gouker, and William D. Oliver. Fabrication process and properties of fully-planarized deep-submicron nb/al–AlO_x/Nb josephson junctions for vlsi circuits. *IEEE Transactions on Applied Superconductivity*, 25(3): 1–12, Jun 2015. ISSN 1558-2515. doi: 10.1109/tasc.2014.2374836. URL `http://dx.doi.org/10.1109/TASC.2014.2374836`.

[42] Niklas Wadefalk, Anders Mellberg, Iltcho Angelov, Michael Barsky, Stacey Bui, Emmanuil Choumas, Ronald Grundbacher, Erik Kollberg, Robin Lai, Niklas Rorsman, Piotr Starski, Jörgen Stenarson, Dwight Streit, and Herbert Zirath. Cryogenic wide-band ultra-low-noise if amplifiers operating at ultra-low dc power. *Microwave Theory and Techniques, IEEE Transactions on*, 51:1705 – 1711, 07 2003. doi: 10.1109/TMTT.2003.812570.

[43] Andreas Wallraff, A. Lukashenko, C. Coqui, Alexander Kemp, Timothy Duty, and AV Ustinov. Switching current measurements of large area josephson tunnel junctions. *Review of Scientific Instruments*, 74, 08 2003. doi: 10.1063/1.1588752.

[44] T. C. White, J. Y. Mutus, I. C. Hoi, R. Barends, B. Campbell, Yu Chen, Z. Chen, B. Chiaro, A. Dunsworth, E. Jeffrey, J. Kelly, A. Megrant, C. Neill, P. J. J. O'Malley, P. Roushan, D. Sank, A. Vainsencher, J. Wenner, S. Chaudhuri, J. Gao, and John M. Martinis. Traveling wave parametric amplifier with josephson junctions using minimal resonator phase matching, 2015.

[45] journal = Chinese Physics B year = 2013 volume = 22 issue = 6 Wu Yu-Lin, title = Fabrication of Al/AlOx/Al Josephson junctions and superconducting quantum circuits by shadow evaporation and a dynamic oxidation process.

[46] A. B. Zorin, M. Khabipov, J. Dietel, and R. Dolata. Traveling-wave parametric amplifier based on three-wave mixing in a josephson metamaterial, 2017.

[47] A.B. Zorin. Flux-driven josephson traveling-wave parametric amplifier. *Physical Review Applied*, 12(4), Oct 2019. ISSN 2331-7019. doi: 10.1103/physrevapplied.12.044051. URL `http://dx.doi.org/10.1103/PhysRevApplied.12.044051`.